Vanishing re-entrance in out-of-equilibrium long-range interacting systems subject to external magnetic field

O. Bulgakova

University of Nova Gorica, Vipavska 13, SI-5000 Nova Gorica

Abstract

Systems with long-range interactions display a short-time relaxation towards quasi-stationary states (QSSs), whose lifetime increases with the system size. To study these states and other peculiar phenomena of long-range interacting systems, the out-of-equilibrium mean-field dynamics of a model for wave-particle interaction is investigated. We consider a paradigmatic model describing the one-dimensional motion of N rotators coupled through a mean-field interaction, and subject to the perturbation of an external magnetic field. The Hamiltonian mean-field model for isolated system was generalized by extending standard Hamiltonian. We follow the dynamics of the order parameter and compare it with the results obtained for the isolated system. Studying the behavior of phase re-entrances in the extended model showed totally different picture as compared with one of no external perturbation. In fact, we obtained that there are no phase re-entrances in the systems subject to the magnetic field.

Keywords: Long-range interacting system, mean-field, quasi-stationary state

Email address: `olga.bulgakova@ung.si` (O. Bulgakova)

1. Introduction

To the present time long-range interactions (LRI) have been shown to be central in astrophysics, hydrodynamics and nuclear physics. In systems with long-range interactions, the two-body potential decays at large distances as $V(r) \propto 1/r^{\alpha}$ with $\alpha \leq d$, where r is scalar distance between the two elements, d is the space dimension. The interest to such systems stems from their ubiquitous presence in nature, and from the fact that their dynamical and statistical behavior is far from being completely understood. Although such systems can be made extensive, they are intrinsically non-additive: the sum of the energies of macroscopic sub-systems is not equal to the energy of the whole system. The violation of this basic property of the thermodynamics of short-range systems is at the origin of new phenomena, such as ensemble inequivalence, negative specific heat in the microcanonical ensemble, and temperature jumps at microcanonical first order phase transitions [1, 4]. In this paper the behavior of the system out-of-equilibrium subject to external magnetic field is studied. As a paradigmatic system on which many theoretical studies focused, we consider the so-called Hamiltonian mean-field (HMF) model [2] which describes one-dimensional motion of N coupled rotators and is characterized by the following Hamiltonian:

$$H = \frac{1}{2} \sum_{j=1}^{N} p_j^2 + \frac{1}{2N} \sum_{i,j=1}^{N} [1 - cos(\theta_j - \theta_i)] \tag{1}$$

where θ_j represents the orientation of the j-th rotor and p_j is its conjugate momentum. In statistical physics, phase re-entrance is a quite typical phenomenon occuring in many physical systems [2], which means the transformation of a thermodynamic system from one phase or state of matter to another and back. In this paper we show how external perturbation of long-range interacting system influences on the existence of phase re-entrances in it.

2. Modeling

The HMF is exactly solvable both in the canonical and microcanonical ensembles, leading in this case to equivalent results, and displays a second order phase transitions from homogeneous to magnetized distributions. Let us modify the HMF model by adding an extra-term which describes the

external magnetic-like field. Such model is mathematically defined by the following Hamiltonian:

$$H = \frac{1}{2} \sum_{j=1}^{N} p_j^2 + \frac{1}{2N} \sum_{i,j=1}^{N} [1 - cos(\theta_j - \theta_i)] - \frac{h}{N} \sum_{j=1}^{N} cos(\theta_j) \qquad (2)$$

where the parameter h is a scalar quantity, which measures the strength of the magnetic field. The equations of motion follow from (2) and read:

$$\dot{\theta}_i = p_i \qquad (3)$$

$$\dot{p}_i = -\frac{1}{N} \sum_{j=1}^{N} sin(\theta_i - \theta_j) - \frac{h}{N} cos(\theta_i) \qquad (4)$$

The HMF is only integrable in the limit of large (resp. vanishing) energy [7]. Hence, to investigate its dynamics one has to perform direct (microcanonical) numerical simulations of equations (3) and (4). To this purpose we have utilized a 4th-order symplectic scheme, with a time step $\tau = 10^{-1}$. To monitor the evolution of the system, it is customary to to introduce the magnetization, a macroscopic order parameter defined as $M = |\mathbf{M}| = |\sum m_i|/N$, where $m_i = (cos\theta_i, sin\theta_i)$ stands for the macroscopic magnetization vector.

The principal motivation that has made HMF model so popular refers to its dynamical features. As previously reported [1, 5, 6] for $h = 0$ (HMF-model), when performing numerical simulations starting out-of-equilibrium, after an initial transient ("transitory" regime) the system gets trapped into QSS's (quasi-stationary states). This can be demonstrated by plotting the magnetization dynamics in time using Molecular Dynamics (MD) numerical simulation, as displayed in fig. 1 [3]. Similarly QSS's are also encountered in the generalized model with $h \neq 0$. Figure 1 shows that the initial evolution towards the QSS is very fast and independent on the system size, but on the other hand, the time duration T_{QSS} of the QSS's diverges with the number of particles N involved. A numerical estimate of T_{QSS} as a function of N is correctly approximated by a power law profile $T_{QSS} \propto N^{\nu}$, with $\nu = 1.7$ [6]. We have focused on "Water Bag" initial conditions, which correspond to a uniformly occupied rectangle in the phase space:

$$f(\theta, p, 0) = f_0 = 1/(4\Delta\theta\Delta p), \text{ if } -\Delta p \leq p \leq \Delta p \text{ and } -\Delta\theta \leq \theta \leq \Delta\theta$$

$$f(\theta, p, 0) = 0, \text{ otherwise.}$$

With this choice, one can express the initial energy density $U = H/N$ and the initial magnetization as functions of $\Delta\theta$ and Δp:

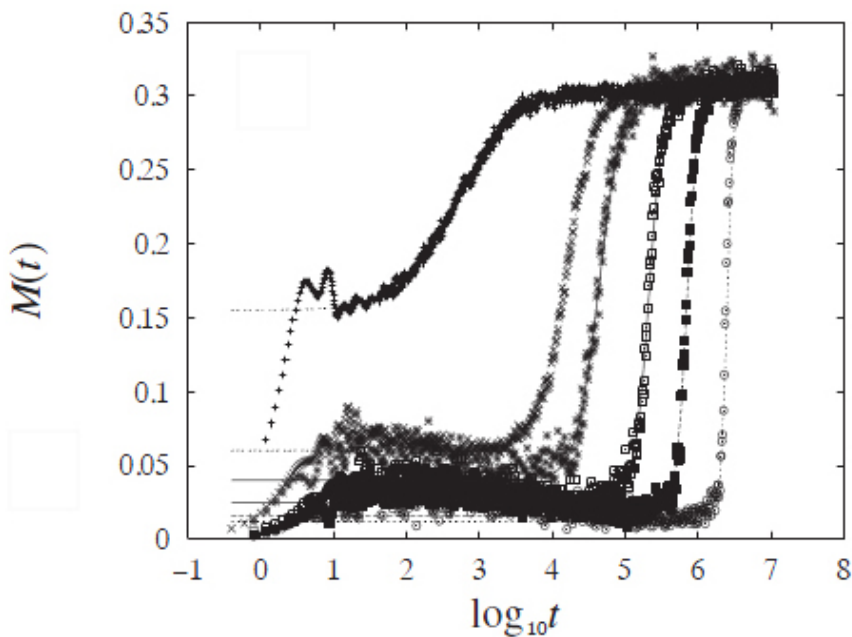$$M_0 = \frac{\sin(\Delta\theta)}{\Delta\theta}, \; U = \frac{(\Delta p)^2}{6} + \frac{1-(M_0)^2}{2}.$$

Figure 1: Temporal evolution of magnetization $M(t)$ for different system sizes: $N = 10^2$, $N = 10^3$, $N = 2 \cdot 10^3$, $N = 5 \cdot 10^3$, $N = 10^4$ and $N = 2 \cdot 10^4$ from left to right.

3. Numerical results

To calculate the generalized HMF model on the computer the programme-code written in Fortran language was used. While running the simulations, different parameters of system and model were varying. To obtain correct averaged results simulations were run for 10 realizations, so the value of magnetization could be averaged in time above different realizations. As
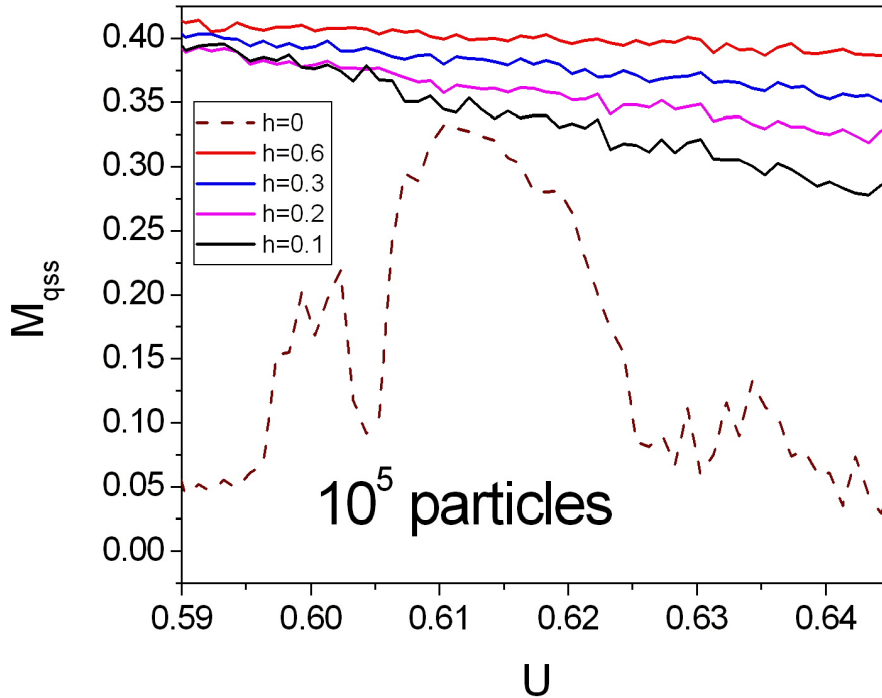
Figure 2: Magnetization at the quasi-stationary state as a function of energy density for different values of magnetic field h and $N = 10^5$. Solid lines represent the behavior of magnetization for non-zero values of magnetic field. The dashed line corresponds to the zero magnetic field.

it was written above, before system gets into QSS the magnetization value strongly arises. Because of this fact, to get adequate results the "transitory" regime was skipped.

Recent simulations [3] showed the existence of a regime of phase re-entrance for isolated long-range interacting systems. Figure 2 shows that the system subject to the magnetic field does not experience the phase re-entrance, as it does when there is no magnetic field. The existence of two rather strong regimes of phase re-entrance can be seen for isolated system. Dashed line shows that for values of energy density around 0.595 and 0.605 the system changes from non-magnetized to magnetized state and back. However, addition of the external magnetic field changes this picture. The mag-

netization depending on the energy density at the quasi-stationary state behaves in the monotonous way, which means that there is no phase transitions at all. Varying parameters of the model and values characterizing the system has not changed the picture drastically. The absence of phase re-entrances has been showed for different values of system-size, initial conditions, time duration.

4. Discussion and conclusions

In this letter the paradigmatic model of LRI system, perturbed by an external magnetic field has been presented. The difference in the behavior of quasi-stationary states for the cases of isolated system and the system subject to external magnetic field has been shown by following the dynamics of magnetization in quasi-stationary state as a function of energy density. The absence of phase re-entrance has been showed for the case of perturbed system. This result draws the picture which is closer to real situations. In a very theoretical case, when there is no external perturbation, the change from non-magnetized state to magnetized is possible. But even small external force can cause the vanishing of any phase transition.

References

[1] R. Bachelard, T. Manos, P. de Buyl, F. Staniscia, F.S. Cataliotti, G. De Ninno, D. Fanelli and N. Piovella. *Experimental perspectives for systems based on long-range interactions*, Journal of Statistical Mechanics: Theory and Experiment, 70 pp. 1261–1272, 2008.

[2] M. Antoni and S. Ruffo. *Clustering and relaxation in Hamiltonian long-range dynamics*, Phys. Rev. E 52, 2361, 1995.

[3] F. Staniscia, P.H. Chavanis, G. De Ninno and D. Fanelli. *Out-of-equilibrium phase re-entrance(s) in long-range interacting systems*, Phys. Rev. E 80, 021138, 2009.

[4] A. Campa, T. Dauxois and S. Ruffo. *Statistical mechanics and dynamics of solvable models with long-range interactions*, Physics Reports 480, 57, 2009.

[5] A. Antoniazzi, D. Fanelli, J. Barre, P.H. Chavanis, T. Dauxois and S. Ruffo. *A maximum entropy principle explains quasi-stationary states in systems with long range interactions: the exemple of the HMF model.* Phys. Rev. E 75, 011112, 2007.

[6] Y.Y. Yamaguchi, J. Barre, F. Bouchet, T. Dauxois and S. Ruffo. *Stability criteria of the Vlasov equation and quasi-stationary states of the HMF model.* Physica A 337, 36, 2004.

[7] A. Antoniazzi, G. De Ninno, D. Fanelli and S. Ruffo. *Wave-plasma interaction: from Plasma Physics to Free-electron.* J. Phys.: Conf. Ser. 7, 143-153, 2005.

Synthesis and optoelectronic characteristics of (Bi,Nd)VO$_4$ photocatalyst

Mirela Dragomir, Matjaz Valant

University of Nova Gorica, Vipavska 13, SI-5000 Nova Gorica, Slovenia

Abstract

Solid solutions of BiVO$_4$ and NdVO$_4$ were synthesized by solid state method. The structural and optical properties of the as prepared samples were studied by several techniques: the phase composition and crystallographic details were obtained from x-ray powder diffraction, the band gaps were determined from diffuse reflectance spectroscopy, and the photoluminescence properties were studied by fluorescence spectroscopy. The results revealed that bismuth has a higher solubility limit in NdVO$_4$ compared with neodymium in BiVO$_4$, and that the band gap of NdVO$_4$ can be tuned by controlling the bismuth doping concentration. We have also found that these materials exhibit interesting optical properties in the field of light emitting devices.

Keywords:
Photocatalyst, Nd-doped BiVO$_4$, Bi-doped NdVO$_4$, solid solutions.

1. Introduction

In the context of increasing energy demands, the enormous amount of clean and free energy offered by the sun is not yet exploited enough. Therefore, a considerable attention is directed toward solar energy conversion technologies such as: hydrogen production by water splitting [1, 2], photocatalytic water purification [3], self-cleaning coatings, or highly efficiency solar cells. Thus, photocatalysis is expected to make a great contribution to environmental treatment and renewable energy.

Photocatalysts are typically metal oxides (e.g. TiO$_2$, VO$_2$, W$_2$O$_3$) metal sulfides (e.g. ZnS, CdS), oxysulfides or oxynitrides (e.g. Sm$_2$Ti$_2$S$_2$O$_5$, TaON),

and composites thereof [4]. The structural and optoelectronic properties of semiconductor photocatalysts determine the efficiency of the photocatalytic process, including the absorption of photons, charge separation and migration, and surface reactions. A semiconductor consists of a valence band and a conduction band, which are separated from one another by a band gap. [5]. Under iradiation by photons with energy equivalent to or larger than Eg, some of the electrons are excited from the valence band to the conduction band, leaving empty states (called holes) in the valence band. These photo-generated electrons and holes may recombine in the bulk or on the surface of the semiconductor. But the electrons and holes that travel to the surface before their recombination cause reduction and oxidation reactions.

Nowadays, the greatest challenge in the quest for visible light active photocatalysts for clean energy and environmental applications is to increase the efficiency of solar light utilization, by absorbing visible light. Most of the photocatalysts developed so far are wide band gap semiconductors, which are active under ultraviolet (UV) light irradiation [6]. Therefore, they can only use a very small portion of sunlight, and their efficiency under solar light irradiation is very low, because the solar spectrum consists of only 4% of UV light. The visible region is far more abundant - 47%, and a visible light active photocatalyst will use a much larger region of the solar spectrum, increasing the efficiency. In the search for efficient visible light active materials, several approaches are taken, such as: finding new single phase materials, tuning the bang gap of the actual UV active photocatalysts by anion or cation doping, decorating UV photocatalysts with a photosensitizer absorbing visible light, fabricating composite photocatalysts, or forming solid solutions between a wide and a narrow band gap photocatalyst.

Engineering the band gap and band positions is crucial in developing visible light responsive photocatalysts. In this study we aimed to prepare solid solutions between two known photocatalysts, bismuth vanadate ($BiVO_4$) and neodymium orthovanadate ($NdVO_4$), in order to tune their energy gap by controlling the composition, and to investigate their electrical and optical properties. $BiVO_4$ is a well known visible light photocatalyst material (Eg = 2.4 eV), mostly used for organic pollutant decomposition and for oxygen evolution in water splitting reaction [7, 8, 9]. But important drawbacks, like low photocatalytic activity and unsuitable conduction band position limits its utilization for hydrogen production and water purification [10]. However, doping $BiVO_4$ with metals [11] has been shown to be effective in the enhancement of its photocatalytic properties. On the other side, $NdVO_4$ is a

very good catalyst and recently was used as photocatalyst for organic pollutant decomposition under UV light irradiation [12]. However, because of its wide band gap (3.4 eV) and low photocatalytic activity, $NdVO_4$ cannot be used for visible light driven photocatalysis [13]. Recently was shown that doping $NdVO_4$ with metals leads to a higher photocatalytic activity under ultraviolet as well as visible light irradiation [14]. But the effect of bismuth doping on the optoelectronic and photocatalytic behaviour of $NdVO_4$ was not studied yet. Taking into account the electronic structure of $BiVO_4$ [15], if a solid solution between $NdVO_4$ and $BiVO_4$ will form, we expect that the coupling between Bi 6s and O 2p orbitals will create a level above the valence band of $NdVO_4$ reducing its band gap for visible light absorption, and would facilitate the hole mobility in $BiVO_4$, increasing in this way their efficiency under solar light irradiation.

2. Materials and methods

We have synthesized by solid state reactions a number of solid solutions of $NdVO_4$ and $BiVO_4$. The composition ratios are: $Bi_xNd_{1-x}VO_4$ (x = 0, 0.1, 0.4, 0.45, 0.48, 0.5, and 0.6) and $Nd_yBi_{1-y}VO_4$ (y = 0, 0.05, 0.08, and 0.1). The analyzed compositions are presented in figure 1.

Stoichiometric amounts of Bi_2O_3 (Alfa aesar, 99.975% purity), V_2O_5 (Alfa aesar, 99.6% purity) and Nd_2O_3 (Alfa aesar, 99.6% purity) were homogenized in a planetary mill using ethanol as homogenizing medium. The powders were then dried and pressed into pellets. The Bi-doped $NdVO_4$ samples were further calcinated in air in 2 steps, at 700°C for 3 h, and 800°C for 3 h, respectively. For the Nd-doped $BiVO_4$ samples, the thermal treatment was done in air at 800°C for 10 h.

The synthesized compounds were characterized for crystal structure and phase composition by means of x-ray powder diffraction (XRD), using a Panalitcal x-ray diffractometer with Cu K_α radiation with a step size of 0.017°. The diffraction patterns were recorded in the range 2θ=10-80°. The optoelectronic properties were determined with different techniques: the band gap was determined from diffuse reflectance measurements by means of diffuse reflectance spectroscopy (DRS). The spectra were recorded with a UV-Vis spectrofotometer[1] in the range 200-800 nm. The photoluminescence
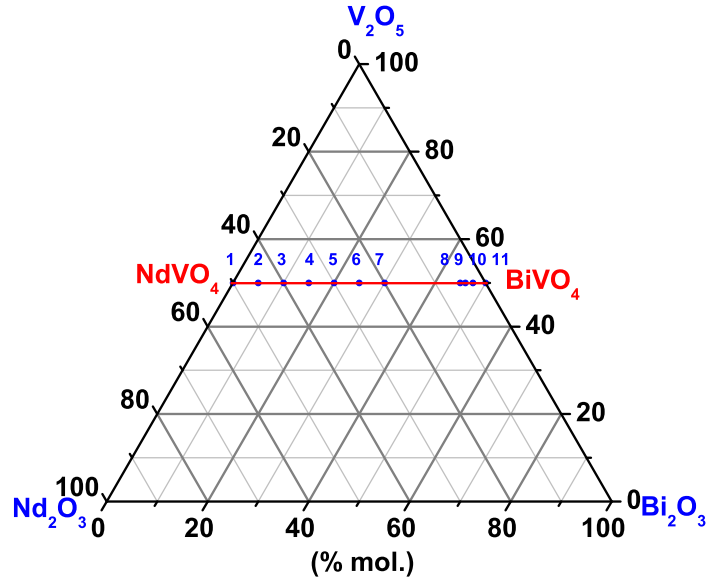
---

[1]Perkin Elmer model λ650S.

Figure 1: Placing the solid solutions in the ternary oxide system: Nd_2O_3 - Bi_2O_3 - V_2O_3. The analysed compositions are denoted with numbers from 1 to 11.

(PL) emission spectra were recorded at room temperature with a 310 nm wavelength excitation source by means of Fluorescence spectroscopy[2].

3. Results and discussion

3.1. X-ray powder diffraction

X-ray powder diffraction analysis was used for identification of the compounds. The XRD patterns in figure 2 show the formation of single phase tetragonal $Bi_xNd_{1-x}VO_4$ compounds for a dopant concentration less than 0.5 mol Bi. In the case where Nd_2O_3 was substituted with Bi concentrations higher than 0.48 mol, beside the main tetragonal phase, peaks of monoclinic $BiVO_4$ were observed in the XRD patterns. These results indicate that for concentrations lower than 0.48 mol, Bi is incorporated in the crystal structure of $NdVO_4$. The XRD pattern for the sample with 0.5 mol Bi show that this concentration is above the solubility limit, because of the formation of

---

[2]with a FL920 fluorescence spectrometer.

4

the secondary phase. These results suggest that the solubility limit x of Bi in $NdVO_4$ is in between 0.48 and 0.5 mol.
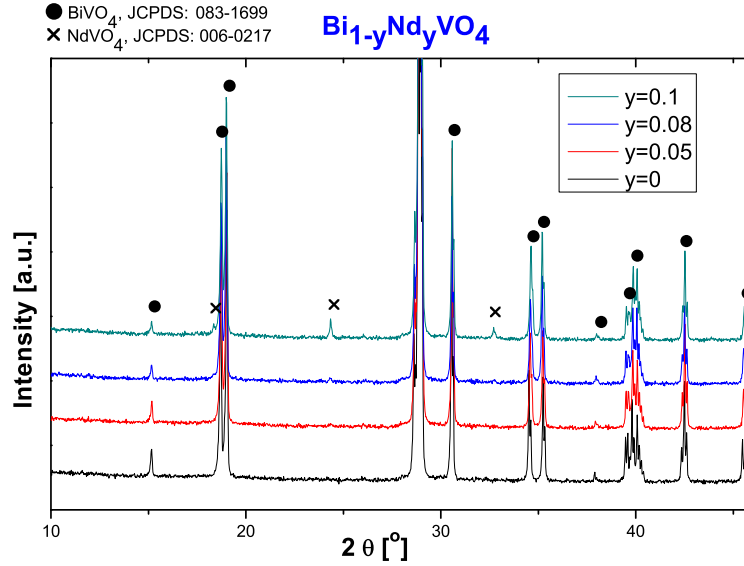

Figure 2: X-ray diffraction patterns for Bi-doped $NdVO_4$ samples with the formula $Nd_{1-x}Bi_xVO_4$. The filled circles denote the tetragonal $NdVO_4$ phase, while the filled triangles represent the monoclinic $BiVO_4$ phase.

The crystallographic details of the $Bi_xNd_{1-x}VO_4$ samples obtained after Rietvelt refinement are presented in figure 3. As the composition of the solid solution changes, the lattice constants of the solid solution also change. For substitutional solid solutions, the lattice constants, and therefore the unit cell volume, often vary in a linear trend with composition. This is called Vegard's law [16]. We observe that the $NdVO_4$ unit cell volume decrease in a linear fashion with the dopant concentration, till 0.48 mol Bi. For concentrations higher than 0.48 mol Bi, the unit cell volume remained constant, in good agreement with Vegard's law of solid solutions.

For the $Nd_{1-y}Bi_yVO_4$ compounds, the XRD patterns presented in figure 4 show that when $BiVO_4$ was doped with Nd concentrations less than 0.08 mol, only single phase monoclinic $Bi_xNd_{1-x}VO_4$ was detected. When the dopant concentration was higher than 0.08 mol, beside the main monoclinic phase, peaks of tetragonal $NdVO_4$ were observed in the XRD patterns. This indicated that Nd can enter in the crystal structure of $BiVO_4$ only till the solubility limit which is in between 0.1 - 0.08 mol.
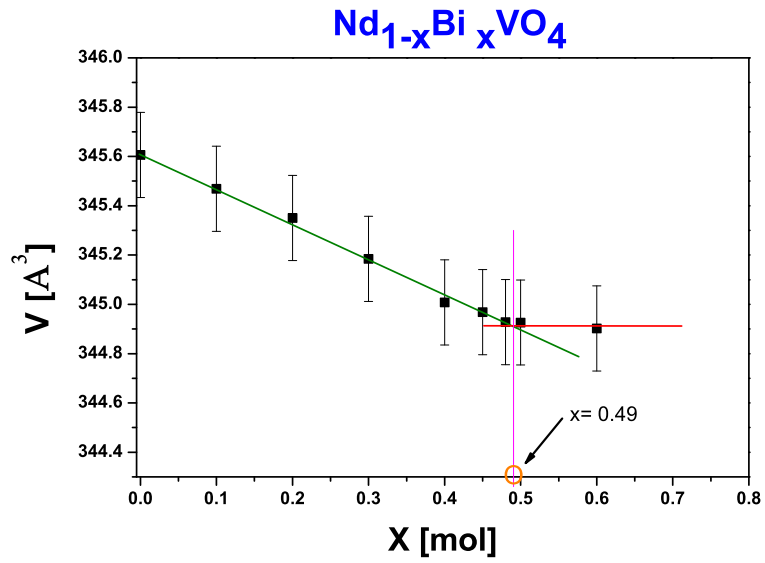
Figure 3: Unit cell variation of $Bi_xNd_{1-x}VO_4$ samples as a function of Bi concentration (x). The unit cell volume (V) of $NdVO_4$ decreases with the Bi-doping until the solubility limit, after the limit it remains constant.
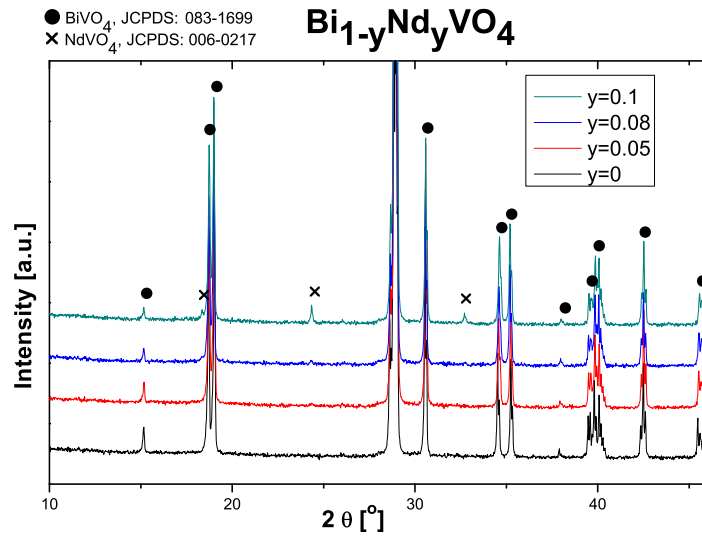

Figure 4: X-ray diffraction patterns for Nd-doped $BiVO_4$ samples. Tetragonal $NdVO_4$ phase is represented with x, while the monoclinic $BiVO_4$ phase is represented with filled circles.

6

3.2. Band gap measurements

UV-Vis diffuse reflectance spectroscopy was used to determine the band gap of Bi-doped $NdVO_4$ and Nd-doped $BiVO_4$ samples. The diffuse reflectance spectra after the Kubelka-Munk treatment [17] are presented in figure 5. The reflectance data were converted into absorption coefficients $F(R_\infty)$. Plotting the square root of the values of absorption coefficients against excitation energy, allows to evaluate the band gap energy - the intersection between the linear fit of the absorption edge and the photon energy axis gives the band gap value.

We observe that pure $NdVO_4$ has a band gap of 3.45 eV and that samples with different Bi-doping concentrations have different band gap energies between 3.13 and 2.99 eV. So, by Bi doping the band gap decreased till 2.99 eV for 0.4 mol Bi doping. The decrease is very accentuated for 0.1 mol Bi, while for concentration higher than 0.2 mol, the decrease is very small. The shift of the band gap to lower energies can be ascribed to the coupling between Bi 6s and O 2p orbitals with the formation of a level above the valence band of $NdVO_4$, reducing in this way the band gap for visible light absorption.
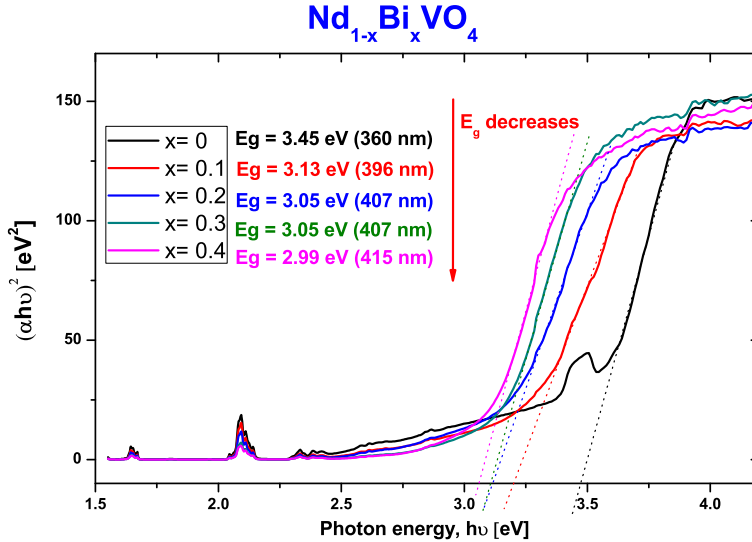

Figure 5: UV-Vis diffuse reflectance spectra of $Bi_{1-x}Nd_xVO_4$ compounds, x = 0, 0.1, 0.2, 0.3, and 0.4. The Kubelka-Munk function is plotted versus the excitation energy.The band gap (Eg) of $NdVO_4$ decreases by Bi-doping.
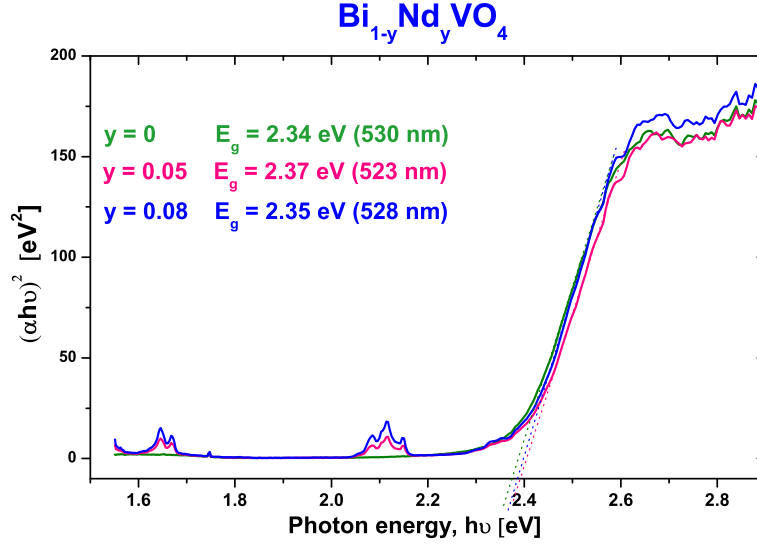
7

Figure 6: UV-Vis diffuse reflectance spectra of $Nd_{1-y}Bi_yVO_4$ compounds. The Kubelka-Munk function is plotted versus the excitation energy. The band gap (Eg) of $BiVO_4$ varies insignificantly with Nd-doping concentration.

In figure 6 are presented the diffuse reflectance spectra of $Nd_{1-y}Bi_yVO_4$ samples. The value of the band gap of monoclinic $BiVO_4$ that we obtained (2.4 eV) is in good agreement with the value reported in the literature [18]. According to the recorded spectra, the band gap of bismuth vanadate varies insignificantly with the dopant (Nd) concentration.

3.3. Fluorescence spectroscopy measurements

As a preliminary analysis before time-domain fluorescence measurements, $NdVO_4$, $BiVO_4$ and Bi-doped $NdVO_4$ samples were characterized in terms of photoluminescence emission spectra, upon excitation with 310 nm, at room temperature. The results are shown in figure 7 a and b.

In the PL spectra, the peaks at 341, 357 and 744 nm were assigned to the charge transfer between V and O in $VO_4{}^{3-}$. The wide peak between 407 and 476 nm is associated with transitions of the 6s electrons of Bi^{3+} to V^{5+} empty orbital. The other peaks from 672, 808 and 833 nm are electronic Nd^{3+} transitions [19]. We observed that the photoluminescence intensity peak of $NdVO_4$ at 341 nm was increased by doping it with Bi, as well as the other 744, 808 and 833 nm peaks. The UV (341 and 357 nm) and red (744 nm)
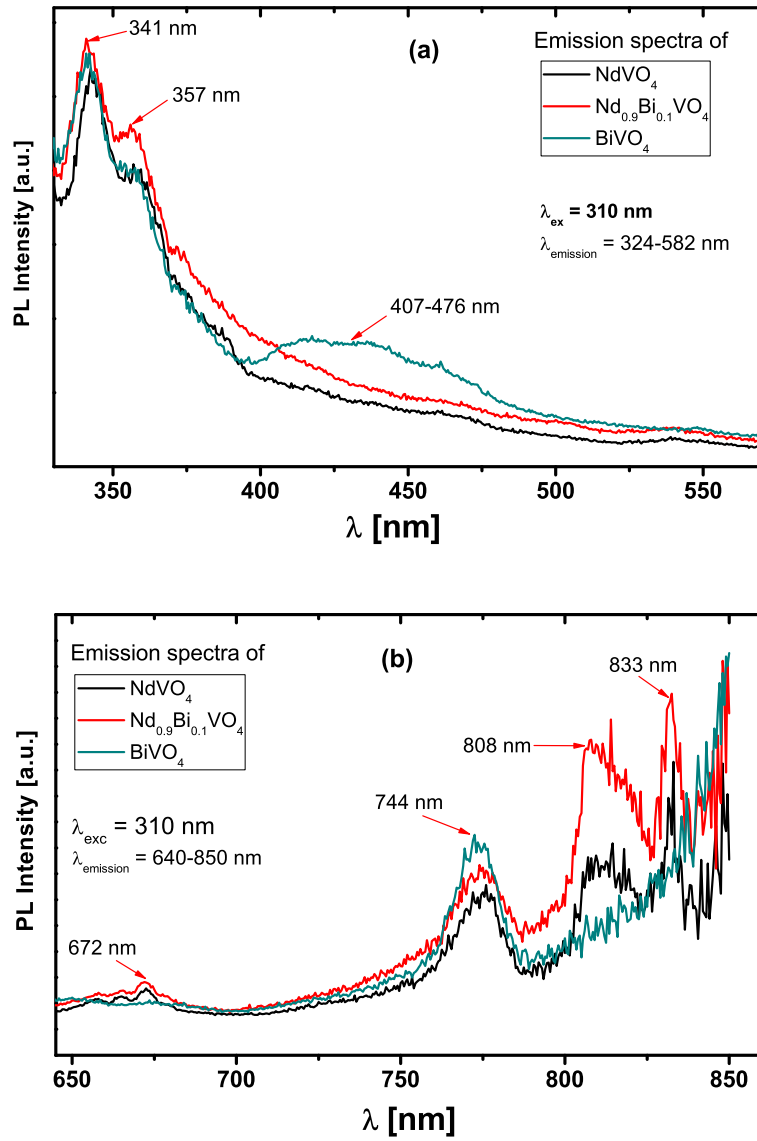
Figure 7: (a,b) Room-temperature photoluminescence spectrum of $Bi_{1-y}Nd_yVO_4$ samples upon excitation with 310nm.

emissions under excitation with 310 nm wavelength, at room temperature, suggest that these compounds cuold be good candidates for UV and red light emitting devices (nanolasers, LEDs).

4. Conclusions

We successfully synthesized for the first time $NdVO_4$ - $BiVO_4$ solid solutions by solid state method, and we analyzed their optoelectronic properties. The results showed that Bi can be incorporated into $NdVO_4$ lattice only till 0.5 mol, while Nd in $BiVO_4$ has a solubility limit in between 0.08 and 0.1 mol. Both solid solutions do not change the crystal structure of the parent compound.

The band gap of $NdVO_4$ decreased with Bi doping. The highest decrease was found for 0.1 mol Bi, value for which the band gap decreased with 0.5 eV, from 3.45 till 2.99 eV. For the Nd-doped $BiVO_4$ samples was not observed any significant variation of the band gap with the dopant concentration. The photoluminescence study of these materials showed that they could be good candidates for UV and red emitting devices (nanolasers, LEDs).

The overall results suggest that $(Bi,Nd)VO_4$ compound has superior optical properties than $BiVO_4$ and $NdVO_4$, and promising photocatalytic properties.

5. Acknowledgement

References

[1] P. Tehsih Yoon, A. Michael Ischay, and J. Du, *Visible light photocatalysis as a green approach to photochemical synthesis*, Nature Chemistry, 2, pp 527-532, 2010.

[2] Z. Zhigang, X. Yinhu, S. Kazuhiro, and A. Hironoi, *Direct splitting of water under visible light irradiation with an oxide semiconductor photocatalysts*, Nature 410, pp 625-627, 2001.

[3] C. Lettman, H. Hinrichs, and M. Maier, *Combinatorial discovery of new photocatalysts for water purification with visible light*, Angewandte Chemie 40, pp 3160-3164, 2001.

[4] J. Zhu and M. Zach, *Nanostructured materials for hydrogen production*, Current Opinion in Colloid and Interface Science 14, pp 260-269, 2009.

[5] Charles Kittel, *Introduction to solid state Physics*, 8th edition, John Wiley and Sons, 2005.

[6] A. Hudo, *Photocatalyst materials for water splitting*, Catalysis Surveys from Asia 7, pp 31-38, 2003.

[7] H. Liu, R. Nakamura, and Y. Nakato, *Promoted photo-oxidation reactivity of particulate BiVO$_4$ photocatalyst prepared by a photoasisted sol-gel method*, Journal of the Electrochemical Society 152, pp 856-861, 2005.

[8] H. Xu, C. Wu, H. Li, G. Sun, J. Xu, and Y. Yan, *Synthesis, characterization and photocatalytic activities of rare earth-loaded BiVO$_4$*, Applied Surface Science 256, pp 597-602, 2009.

[9] A. Zhang and Y. Zhang, *Effects of europium doping on the photocatalytic behaviour of BiVO$_4$*, Journal of Hazardous Materials 173, pp 265-272, 2010.

[10] A. Martinez-de la Cruz and U.M. Garcia Perez, *Photocatalytic properties of BiVO$_4$ prepared by the co-precipitation method: degradation of Rhodamine B and possible reaction mechanism under visible irradiation*, Materials Research Bulletin 45, pp 135-141, 2010.

[11] X. Hui, W. Chundu, L. Huaming, S. Guangsong, X. Yunanguo, and Y. Yongsheng, *Synthesis, characterization and photocatalytic activities of rare earth-loaded BiVO$_4$ catalysts*, Applied Surface Science 296, pp 597-602, 2009.

[12] M. Sudarshan, M. Giridhar, and T.N. Guru, *Microwave synthesis and photocatalytic activity of nano lanthanide (Ce, Pr and Nd) orthovanadates*, Industrial and Engineering Chemistry Research 47, pp 6509-6516, 2008.

[13] R. Selvan, A. Gedanken, P. Anil Kumar, G. Marikadan, and C. Karunakaran, *Synthesis and characterization of rare earth orthovanadate (RVO$_4$; R = La, Ce, Nd, Sm, Em, and Gd) nanorods (nanocrystals) nanospindles by a facile sonochemical method and their catalytic properties*, Journal of Cluster Science 20, pp 291-305, 2009.

[14] M. Sudarshan, M. Giridhar, and T.N. Guru, *Structural and photocatalytic activity of lanthanide (Ce, Pr, and Nd) molybdovanadates*, Journal of Physical Chemistry C 111, pp 6505-6511, 2007.

[15] A. Walsh, Y. Yan, M. N. Huda, M. M. Al-Jassim, and S. Wei, *Band edge electronic structure of $BiVO_4$: elucidating the role of the Bi s and V d orbitals*, Chemistry of Materials 21, pp 547-551, 2009.

[16] K.T. Jacob, S. Raj, and L. Rannesh, *Vegard's law: afundamental relation or an approxination?*, Journal of Materials Research 9, pp 776-779, 2007.

[17] A. Escobedo Morales, E. Sanchez Mora, and U. Pal, *Use of diffuse reflectance spectroscopy for optical characterization of un-supported nanostructures*, Revista Mexicana de Fisica S 53, pp 18-22, 2006.

[18] H. Jiang, H. Endo, H. Natori, M. Nagai, K. Kobayashi, *Fabrication and photoactivities of spherical-shaped $BiVO_4$ photoctalysts through solution combustion synthesis method*, Journal of the European Ceramic Society 28, pp 2955-2962, 2008.

[19] X. Wu, Y. Tao, L. Dong, J. Zhu, *Preparation of single-crystalline $NdVO_4$ nanorods, and their emissions in the ultraviolet and blue under ultraviolet excitation*, The Journal of Physical Chemistry B 109, pp 11544-11547, 2008.

Fully-tunable femtosecond laser source in the ultraviolet spectral range

B. Mahieu

University of Nova Gorica, Vipavska 13, SI-5000 Nova Gorica

Abstract

We demonstrate experimentally the full tunability of a coherent femtosecond source in the whole ultraviolet spectral region. The experiment relies on the technique of high-order harmonic generation driven by a near-infrared parametric laser source in Krypton gas. By tuning the drive wavelength in the range between 1100 to 1900 nm, we generated intense harmonics from near to extreme ultraviolet. A number of photons per shot of the order of 10^7 has been measured for the first harmonic orders. Many novel scientific prospects are expected to get benefit from the use of such a table-top tunable source.

Keywords: High-order Harmonic Generation, Optical Parametric Amplifier, femtosecond, tunability, ultraviolet

1. Introduction

Generating tunable sub-picosecond radiation at wavelengths shorter than 250 nm is of great interest to many applications in physics, chemistry and biology [1, 2, 3], both in gas-phase and condensed matter. In fact, below such a wavelength one overcomes the work function of most solids and clusters of metals and metalloids, making possible to eject electrons from the target sample via optical excitation. Working with short wavelengths is also required for the implementation of high-resolution imaging techniques [4]. The use of short pulses allows to obtain important information on the dynamics of fast processes occurring in systems like proteins, enzymes and nucleic acids [5]. Such a dynamics is often excited in a given small range of wavelengths (typically few nanometers). Hence, "fine" tunability is an important asset of the employed radiation source. A more extended tunability (tens of nanometers) is of course also highly desirable, since it allows the study of a large variety of samples, with the same radiation source.

It is well known that wavelengths below 200 nm are not accessible to conventional lasers, due to the lack of high-reflectivity broadband mirrors and to the decreasing efficiency of harmonic conversion in nonlinear crystals within this spectral range. Also synchrotron radiation is not a viable option, mainly due to the fact that

pulses are limited to picosecond durations. In fact, apart from free-electron lasers [6], the most effective way to obtain femtosecond laser pulses in the ultraviolet and soft X-ray spectral region relies on the technique of high-order harmonic generation (HHG) in gas [7, 8, 9]. The latter is a highly nonlinear process based on the interaction of a noble gas with a visible or infrared (IR) light beam spatially focused so as to reach an intensity of the order of 10^{14} W/cm^2. As an output of such an interaction, a comb of odd harmonics of the laser wavelength is generated. For the first harmonic orders (third, fifth, seventh), the signal falls with the harmonic order and the process is well explained in the frame of classical nonlinear optics in centrosymmetric media [10, 11]. Instead, higher-order harmonics have almost the same intensity, forming a characteristic plateau. The wavelength at which is located the plateau's cut-off is proportional to the square of the fundamental wavelength. The HHG process can be explained by means of the quantum model reported in [12]. However, the main features of the harmonic emission can be accounted for using a semiclassical model [13, 14].

Generally, the drive (fundamental) beam for HHG has a fixed wavelength, most often around 800 nm for a standard Ti:Sapphire source. Thus, harmonic wavelengths are also fixed. As a consequence, especially for low harmonic orders, harmonic peaks are far away from one another. This lack of tunability is a drawback for previously cited scientific applications, reducing optical excitations to a few number of photon energies.

A common technique to improve tunability is to drive HHG with harmonic frequency-mixed laser pulses, such as 800 nm and 400 nm [15]. This allows to generate also pair harmonics of the 800 nm signal, partially filling the gap between spectral lines. However, harmonic peaks remain discrete and fixed. Full tunability have been demonstrated for high harmonic orders, corresponding to harmonic wavelengths in the extreme-ultraviolet (EUV) spectral range, with techniques such as harmonic blueshifting depending on the generation geometry [16], control of the chirp of the drive laser [17] or, in the picosecond range, tuning of a non-compressed narrow-band Ti:Sa drive source over its spectral range of amplification [18]. A more effective solution to get full tunability of a femtosecond harmonic beam is to rely on a widely tunable drive laser. This has been demonstrated for harmonics around 150 nm driven by a near-infrared source tunable from 1200 to 1550 nm with pulse durations larger than 100 fs [19].

In the study described in the present article, we demonstrate experimentally the possibility of obtaining an intense harmonic beam with full tunability over the whole ultraviolet spectral range. This has been possible by the use, for driving HHG, of a source tunable from 1100 to 1900 nm [20]. Moreover, the mJ-level pulses provided by this facility have a duration smaller than 20 fs, ensuring the generation of ultrashort harmonics. In the next section, we describe the implementation of the experiment. Experimental results are then presented and discussed.

2. Experimental setup

The layout of the experiment is shown in Fig. 1. The parametric source relies on a Ti:Sapphire laser facility providing high-energy (tens of mJ) pulses of duration 60 fs, centered at a wavelength of 790 nm, with a repetition rate of 10 Hz. The output beam stems from difference frequency generation (DFG [21]) of spectrally broadened pulses. The generated pulses are then amplified in a two-stage optical parametric amplifier (OPA [22]), leading to the production of 17-fs pulses with an energy up to 1.2 mJ, tunable from 1100 to 1900 nm. The tunability is obtained by changing the phase-matching condition in the crystal used for DFG, which simply consists in rotating it.

The generation of the high-order harmonics of the near-IR driving pulses is achieved by focusing the laser beam in a jet of Krypton gas, which ensures a better harmonic conversion efficiency than lighter gases such as Argon, but with a lower cutoff frequency [23]. After the generation points, the harmonics co-propagate with the generating laser through the instruments that have been used for the spectral analysis respectively in the deep-ultraviolet (DUV) and in the extreme-ultraviolet (EUV) spectral regions. The harmonic emission in the DUV was analyzed through a normal-incidence Czerny-Turner scanning monochromator (McPherson model 218) equipped with a 2400-gr/mm $AlMgF_2$-coated grating. The monochromator carries out the spectral selection of a single harmonic or of a spectral portion of it. The photon flux at the exit slit of the monochromator is detected by a photomultiplier tube (Hamamatsu model R1414) with a TPB phosphor photocathode to enhance the detection efficiency within the whole vacuum-ultraviolet region. Owing to the limited spectral range accessible to the grating, that has an useful efficiency for wavelengths above $\approx$130 nm, only the harmonics ranging from the third to the eleventh order of the fundamental wavelength could be detected. The harmonic spectra with high resolution were obtained through the grating scanning with a 300-μm slit aperture, giving a bandwidth of 0.4 nm per point.

The global response of the instrument (i.e. monochromator and detector) has been absolutely calibrated using the facilities available at CNR-IFN and described in details in [24], in order to measure the DUV photon flux generated in the interaction region at the different harmonics. This was performed by tuning the monochromator to one of the harmonics and opening completely its slits. In such a way, the beam enters into the monochromator without being cut at the entrance slit, then is diffracted by the grating. Finally, the whole harmonics of interest exit from the output slit and is detected by the photomultiplier. It has been previously verified that the different harmonics were clearly separated at the output even with the slits completely open.

The signal in the EUV was analyzed through a grazing-incidence flat-field spectrometer equipped with a 1200-gr/mm gold-coated grating usable in the 80-35 nm spectral region. The spectrum is acquired by a 40-mm-diameter microchannel plate intensifier with MgF_2 photocathode and phosphor output optically coupled with a low-noise CCD camera. Also in this case, the global response of the instrument (i.e. grating and detector) has been absolutely calibrated, as described in details in [25, 26]. Since the spectrometer works without an entrance slit, having the harmonics generation point as its input source, all the generated EUV photons enter into the instrument and are diffracted on the 2-D detector, allowing the simultaneous measurement of the spectrum and intensity in the whole spectral interval covered by the detector.
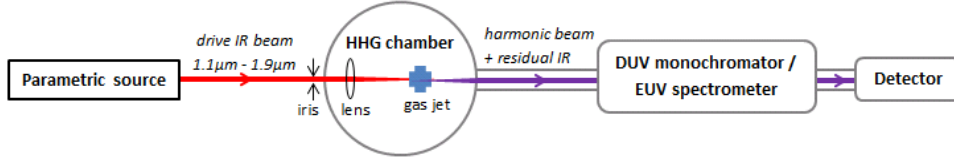
Figure 1: Layout of the experiment. The parametric source, for which a comprehensive description can be found in [20], provides a tunable near-IR drive beam. It is focused with a lens of 15 cm focal length onto a Krypton gas jet at a backing pressure of 3.5 bars. The position of the jet with respect to the laser focus was optimized to give the maximum harmonic yield with a given laser focal spot. This was achieved by carefully adjusting the position of the gas jet with respect to the laser focus by a manual x-y-z translation stage with a precision in the positioning of ±0.1 mm. Moreover, an iris placed on the path of the drive beam allows to adjust size and intensity at the focus so as to avoid gaz ionization. The gas is injected in the HHG chamber through an electromagnetic valve, synchronized with the beam, with a nozzle diameter of 0.5 mm operating with an opening time of 400 μs. The spectrum of the harmonic beam was acquired by two different detection systems: a monochromator in the DUV and a spectrometer in the EUV, with suitable photomultiplier detectors. Detection systems in both DUV and EUV regions have been calibrated so as to calculate the harmonic photon flux.
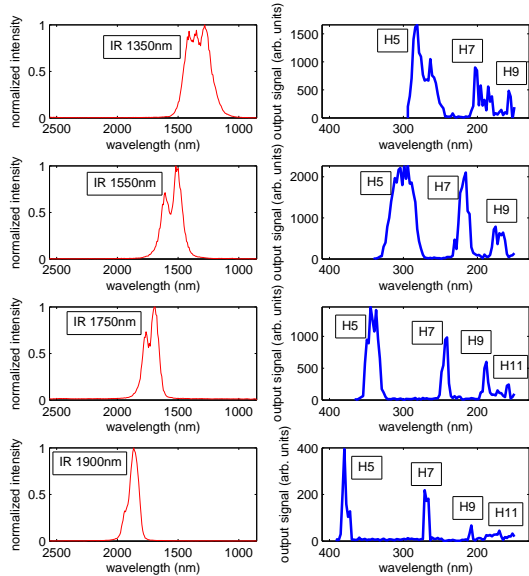

Figure 2: IR spectra (left side) and corresponding harmonic spectra (right side) in the 400 - 150 nm spectral region. H5, H7, H9 and H11 stand respectively for the fifth, seventh, ninth and eleventh harmonics of their drive IR beam.

3. Results and discussions

Deep-ultraviolet (DUV) region

Figure 2 shows the spectral characterization from four sets of measurements, corresponding to four different drive IR wavelengths: 1350, 1550, 1750 and 1900 nm. It is important to stress that the stability of the beam provided by the parametric source ensures a very good reproducibility of the measurements.

Below 150 nm, the efficiency of the DUV monochromator is dramatically low. Thereby, the analysis of harmonic spectra has been done only down to 150 nm. Since the third harmonics of the considered drive IR wavelengths are generally located in the visible, i.e. out of the monochromator range, harmonic orders from fifth to ninth or eleventh have been analyzed. As expected at these relatively low orders, the signal is quickly decreasing as a function of the harmonic order. Indeed, the intensity of harmonics before the plateau region is related to the probability of multiphoton ionization of the gas atoms [27]. As the drive beam, harmonics have a quite large bandwidth (some tens of nanometers), intrinsic to an ultrashort pulse source.

The overlap of the harmonic spectra shows a full tunability of the source in the DUV spectral region (Fig.3). The range between 400 and 350 nm corresponds to either the fifth harmonic of a 1750-2000 nm fundamental beam or the third harmonic of a 1050-1200 nm fundamental beam. These wavelengths are the boundaries of the accessible spectral range of the used parametric source, so that in these regions the IR spectrum is less stable and moreover the beam energy is lower than in the 1350-1550 nm "peak region". Hence harmonics in the 400-350 nm region are also less intense. Nevertheless, in the frame of classical nonlinear optics, the third harmonic of a 1050-1200 nm fundamental beam can be generated for instance by third-order nonlinear process in a potassium dihydrogen phosphate (KDP) crystal, ensuring a better conversion efficiency.

Fig. 4 clearly shows that ranging the drive wavelength from 1350 to 1900 nm, as it has been done in these measurements, harmonic orders from fifth to eleventh completely cover ultraviolet wavelengths down to 100 nm. Furthermore, the third harmonic, not shown in Fig. 4,
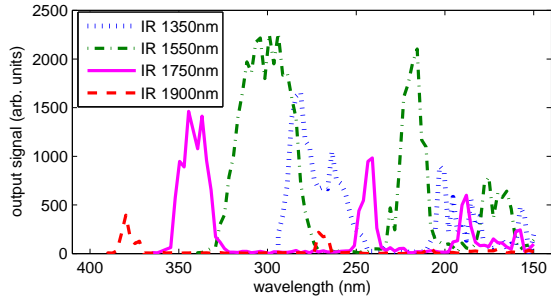
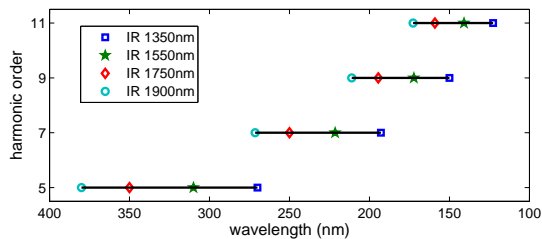Figure 3: Overlap of the harmonic spectra for four drive IR wavelengths (1350, 1550, 1750 and 1900 nm).

Figure 4: Tunability in the DUV. The lines represent the wavelength ranges that are covered by harmonic orders from fifth to eleventh, generated by drive wavelengths ranging from 1350 nm to 1900 nm.

also allow tunability from the visible region. Obviously, going towards shorter wavelengths, this overlap and thereby the tunability in the ultraviolet range is improved. Hence, narrower IR tunability is sufficient at lower wavelengths.

The photon flux of the harmonics has been measured by fully opening the slits of the monochromator in order to get all the signal on the photomultiplier. The results are summarized in Table 1. Around 10^7 photons per shot are generated in and around the DUV spectral region, corresponding to a beam energy of the order of 10 pJ. One sees that the higher the drive wavelength, the smaller the harmonic photon flux. Regarding the ninth harmonic of the drive laser (which can be considered as the first plateau harmonic) for 1350, 1450 and 1800 nm drive wavelengths (λ_{IR}), the harmonic conversion efficiency is scaled as $\lambda_{IR}^{-6.34}$. This is in agreement with recent theoretical studies, in which it was shown that the harmonic efficiency in the plateau region scales as λ_{IR}^{-6}, and not as λ_{IR}^{-3}, as previously believed [28]. Moreover, in [29], the conversion efficiency of further plateau harmonics (from 78 to 39 nm) has recently been measured to be proportional to $\lambda_{IR}^{-6\pm1.1}$ in Krypton. Although increasing the drive wavelength allows to extend the harmonic plateau [30], there is a drawback in terms of har-

Table 1: Absolute number of photons provided in the DUV spectral range for four different drive wavelengths. First column: approximate central wavelength of the drive beam; second column: wavelengths corresponding to the peak signal of the harmonics; third column: measured photons/harmonic/shot for each harmonic.

drive IR	harmonics	photons/harmonic/shot
1160 nm	414 nm	$2.0 \cdot 10^8$
	248 nm	$6.1 \cdot 10^7$
	177 nm	$3.6 \cdot 10^7$
1350 nm	270 nm	$4.2 \cdot 10^7$
	196 nm	$1.8 \cdot 10^7$
	153 nm	$1.3 \cdot 10^7$
1450 nm	285 nm	$6.1 \cdot 10^7$
	204 nm	$1.6 \cdot 10^7$
	161 nm	$8.2 \cdot 10^6$
1800 nm	267 nm	$1.3 \cdot 10^7$
	262 nm	$7.0 \cdot 10^6$
	206 nm	$3.4 \cdot 10^6$

monic efficiency.

Extreme-ultraviolet (EUV) region

The same characterization procedure as in the DUV has been followed for the measurements performed in the EUV region, using the suitable detection system described previously. Harmonic spectra are reported in Fig. 5 for three different drive wavelengths (1350, 1450 and 1550 nm) and their overlap in the 45-35 nm spectral range is shown in Fig. 6. One can see, especially for the 1550 nm drive wavelength, that harmonic spectra reach their cutoff in this region. Fig. 7 shows that ranging the drive wavelength from 1350 nm to 1550 nm is enough for getting the full tunability in the EUV, through relatively high-order harmonics. One interesting point is that one specific ultraviolet wavelength can be obtained by numerous drive wavelengths through different harmonic orders.

The absolute number of photons in the EUV is stated in Table 2 for harmonic orders 21, 29 and 35 of 1350, 1450 and 1550 nm drive wavelengths. Such photon flux correspond to an energy per harmonic per shot of about two orders of magnitude less than in the DUV. First of all, it can be explained by the fact that less IR energy has been used here for driving HHG. We estimate at about 270 μJ the energy of the drive pulses at a wavelength of 1450 nm, i.e. about 3 times less than in previous measurements. Such a low IR energy involves a decrease of the phase-matching quality thus of the macroscopic construction of harmonics, and of their final flux. Moreover, as said previously, harmonics generated in Krypton reach their cutoff region in the EUV. But a lighter
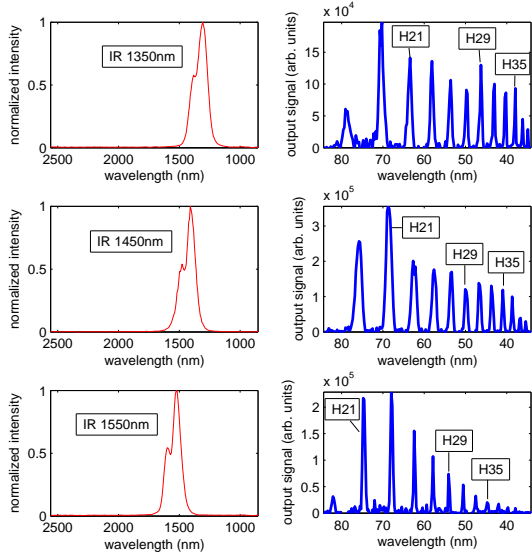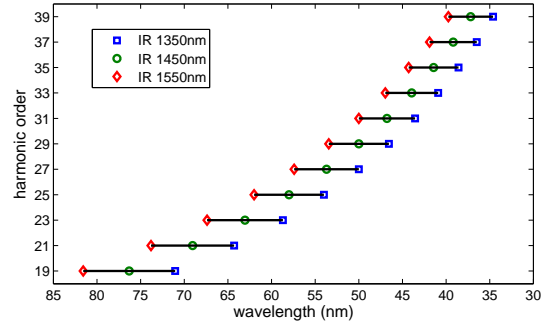
Figure 7: Tunability in the EUV. The lines represent the wavelength ranges that are covered by harmonic orders from number nineteen to thirty-nine, generated by drive wavelengths ranging from 1350 nm to 1550 nm.

Table 2: Absolute number of photons provided in the EUV spectral range for three different drive wavelengths. First column: approximate central wavelength of the drive beam; second column: wavelengths of harmonic orders 21, 29 and 35; third column: measured photons/harmonic/shot for each harmonic.

drive IR	harmonics	photons/harmonic/shot
1350 nm	63 nm	$1.3 \cdot 10^4$
	46 nm	$5.8 \cdot 10^3$
	38 nm	$2.8 \cdot 10^3$
1450 nm	69 nm	$4.4 \cdot 10^4$
	50 nm	$9.9 \cdot 10^3$
	41 nm	$4.7 \cdot 10^3$
1550 nm	75 nm	$1.4 \cdot 10^4$
	54 nm	$3.1 \cdot 10^3$
	45 nm	$6.5 \cdot 10^2$

Figure 5: IR spectra (left side) and corresponding harmonic spectra (right side) in the 85 - 30 nm spectral region. H21, H29 and H35 stand respectively for harmonic orders number twenty one, twenty nine and thirty five of their drive IR beam.
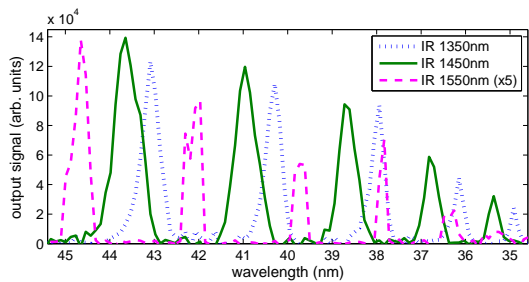
Figure 6: Overlap of the harmonic spectra in the range 45 - 35 nm for three drive IR wavelengths (1350, 1450 and 1550 nm). The harmonic spectrum resulting from a drive wavelength of 1550 nm has been heightened.

gas can be used in order to increase the cutoff frequency, with the drawback of a lower efficiency in the plateau region.

Different ways can be studied to overcome this low photon flux. As a first possibility, one could design a more powerful parametric source. This could mean higher energy per pulse like in [31], higher repetition rate and not necessarily such a wide tunable spectral range. Indeed, it is clear in Fig. 4 and Fig. 7 that changing the drive wavelength from 1350 to 1750 nm already allows to get the full tunability from 350 nm down to shorter harmonic wavelengths. A possible alternative or complement is the enhancement of the HHG process. In this respect, a promising technique that could be investigated is based on mixing the parametric source with a standard powerful Ti:Sa laser one, forming non-collinear drive wavelengths [32].

5

4. Conclusion

The full tunability of a femtosecond laser beam produced through HHG driven by a parametric source has been demonstrated in the whole ultraviolet spectral range. This source opens the way to novel scientific experiments. The main drawback comes from the relatively low harmonic conversion efficiency, resulting from a drive wavelength longer than in classic HHG setups. Increasing the harmonic photon flux would bring benefit for previously cited scientific applications, and possibly for the development of a tunable ultraviolet and soft X-ray source for seeding of free-electron lasers, where HHG-based sources have demonstrate to be an attractive prospect [33].

References

[1] M. Marsi et al., *UV/VUV free electron laser oscillators and applications in materials science*, Surf. Rev. Lett. 9, 599, 2002.

[2] R. Neutze et al., *Potential for biomolecular imaging with femtosecond X-ray pulses*, Nature 406, 757, 2000.

[3] M. Giglio, M. Carpineti, and A. Vailati, *Space intensity correlations in the near field of the scattered light: a direct measurement of the density correlation function g (r)*, Phys. Rev. Lett. 85, 1416, 2000.

[4] H. N. Chapman et al., *Femtosecond time-delay X-ray holography*, Nature 448 676, 2007.

[5] G. S. Edwards et al., *Applications of Free-Electron Lasers in the Biological and Material Sciences*, Photochem. and Photobio. 81, 711, 2005.

[6] Patrick G. O'Shea and Henry P. Freund, *Free-Electron Lasers: Status and Applications*, Science vol. 292, 2001.

[7] P. Salières et al., *Study of the spatial and temporal coherence of high order harmonics*, Adv. At. Mol. Opt. Phys. 41, 83-142, 1999.

[8] P. Jaeglé, *Coherent sources of XUV radiation*, Springer, 2006.

[9] T. Brabec and H. Kapteyn, *Strong field laser physics*, Springer, 2008.

[10] G. H. C. New and J. F. Ward, *Optical third-harmonic generation in gases*, Phys. Rev. Lett. 19, 556, 1967.

[11] Y. R. Shen, *Principles of nonlinear optics*, Wiley-Interscience, First Edition, 1984.

[12] M. Lewenstein et al. *Theory of high-harmonic generation by low-frequency laser fields*,Phys. Rev. A 49, 2117, 1994.

[13] P. B. Corkum, *Plasma perspective on strong field multiphoton ionization*, Phys. Rev. Lett. 71, 1994, 1993.

[14] K. J. Schafer et al., *Above threshold ionization beyond the high harmonic cutoff*, Phys. Rev. Lett. 70, 1599, 1993.

[15] G. Lambert et al., *An optimized kHz two-colour high harmonic source for seeding free-electron lasers and plasma-based soft x-ray lasers*, New J. Phys. 11 083033, 2009.

[16] C. Altucci et al., *Tunable soft-x-ray radiation hy high-order harmonic generation*, Phys. Rev. A 61, 21801, 1999.

[17] Kim et al., *Continuously tunable high-order harmonics from atoms in an intense femtosecond laser field*, Phys. Rev. A 67, 051801, 2003.

[18] F. Brandi, D. Neshev and W. Ubachs, *High-Order Harmonic Generation Yielding Tunable Extreme-Ultraviolet Radiation of High Spectral Purity*, Phys. Rev. Lett. 91, 163901, 2003.

[19] M. Bellini, *Generation of widely tunable harmonic pulses in the UV and VUV from a NIR optical parametric amplifier*, Appl. Phys. B 70, 773–776, 2000.

[20] C. Vozzi et al., *Millijoule-level phase-stabilized few-optical-cycle infrared parametric source*, Optics Letters 32, 2957, 2007.

[21] A. Baltuška, T. Fuji, and T. Kobayashi, *Self-referencing of the carrier-envelope slip in a 6-fs visible parametric amplifier*, Opt. Lett. 27, 1241-1243, 2002.

[22] G. Cerullo and S. De Silvestri, *Ultrafast optical parametric amplifiers*, Rev. Sci. Instrum. 74, 1, 2003.

[23] K. C. Kulander and T. N. Rescigno, *Effective potentials for time-dependent calculations of multiphoton processes in atoms*, Computer Physics Communications Volume 63, Issues 1-3, 1991.

[24] L. Poletto, A. Boscolo, and G. Tondello, *Characterization of a Charge-Coupled-Device Detector in the 1100-0.14-nm (1-eV to 9-keV) Spectral Region*, Appl. Opt. 38, 29-36, 1999.

[25] L. Poletto, G. Tondello, and P. Villoresi, Rev. Sci. Instr. 72, 2868-2874 (2001)

[26] L. Poletto, S. Bonora, M. Pascolini, and P. Villoresi, Rev. Sci. Instr. 75, 4413-4418 (2004)

[27] Xiao-Min Tong and Shih-I Chu, *Multiphoton ionization and high-order harmonic generation of He, Ne, and Ar atoms in intense pulsed laser fields: Self-interaction-free time-dependent density-functional theoretical approach*, Phys. Rev. A 64, 013417, 2001.

[28] J. Tate et al., *Scaling of Wave-Packet Dynamics in an Intense Midinfrared Field*, Physical Review Letters / 98, 013901, 2007.

[29] A. D. Shiner et al., *Wavelength Scaling of High Harmonic Generation Efficiency*, Physical Review Letters 103, 073902, 2009.

[30] T. Popmintchev et al., *Extended phase matching of high harmonics driven by mid-infrared light*, Optics Letters / Vol. 33, No. 18, 2008.

[31] E. J. Takahashi et al., *10 mJ class femtosecond optical parametric amplifier for generating soft x-ray harmonics*, Applied Physics Letters 93, 041111, 2008.

[32] J. B. Bertrand et al., *Ultrahigh-Order Wave Mixing in Non-collinear High Harmonic Generation*, Phys. Rev. Lett. 106, 023001, 2011.

[33] G. Lambert et al., *Injection of harmonics generated in gas in a free-electron laser providing intense and coherent extreme-ultraviolet light*, Nature Physics 4, 296 - 300, 2008.

The effect of Fe doping on BaTiO$_3$ crystal structure

I. Mikulska

University of Nova Gorica, Vipavska 13, SI-5000 Nova Gorica

Abstract

Fe doped BaTiO$_3$ was prepared by solid state reaction and post-annealed in oxygen atmosphere. X-ray diffraction analysis indicated that samples with different amount of Fe^{3+} ions have different crystal structure. The X-ray absorption spectroscopic methods XANES and EXAFS were used to retrieve the Fe valence state and local structure around the Fe atoms. The results show that iron octahedraly coordinated by six oxygen atoms and substituted Ti^{4+} sites. No impurities or secondary phases, such as Fe$_2$O$_3$, were found.

Keywords: Fe doped BaTiO$_3$, X-ray absorption spectroscopy, dilute magnetic oxides

1. Introduction

Dilute magnetic oxides (DMO) are materials such as ZnO, SnO_2 and TiO_2 that become ferromagnetic when doped with a few per cent of transition metal ions such as Mn, Fe and Co. These materials hold significant potential for spintronic devices if ferromagnetism can be understood and controlled [1]. However, ferromagnetic behavior in DMO systems is controversial, as numerous reports have claim intrinsic ferromagnetic behavior above room temperature, while a large number of others attribute these room temperature effects to impurities [2–6].

Within this work we focused on ferroelectric material Fe-doped $BaTiO_3$, which is typical representative of dilute magnetic oxides with perovskite structure. Even for this well known material was reported inconsistent results of ferromagnetic behavior. There was a number of reports which claimed doping with a few per cent of Fe^{3+} ions leads to observation of room temperature ferromagnetic behavior in Fe-doped $BaTiO_3$ [2–6]. It was found that $BaTi_{1-x}Fe_xO_3$ ceramics (x =0.07, 0.3 and 0.7) has hexagonal structure and room temperature ferromagnetism was observed for all samples[3,4]. $BaTiO_3$ doped with 10-60% of Fe has pure hexagonal structure. For small amount of iron (x =0.005, 0.01, 0.05, 0.07) it was shown that large single crystals, which were prepared by conventional floating zone technique, have pure hexagonal phase [5]. Samples with 5% and 7% of Fe ions exhibit room temperature ferromagnetism. However, there were shown contrary results that 2% of Fe doped $BaTiO_3$ has pure tetragonal perovskite structure [6]. In spite of numerous reports about room temperature ferromagnetism in Fe-doped $BaTiO_3$ ceramics the nature of this ferromagnetic behavior (intrinsic or extrinsic) still is not clear. Extrinsic ferromagnetism behaves from clusters (Fe_2O_3) or secondary phases in DMO systems [7]. Small clusters can easily show μ=5×10^{-6} emu[1] magnetic moment.

Thus the nature of ferromagnetic behavior of Fe-doped $BaTiO_3$ is not conclusively determined therefore new tests are needed. In case of DMO materials conventional X-ray diffraction technique (XRD) is not sufficient to indicate the existence of small clusters or secondary phases. Thus within this work we used X-ray absorption spectroscopy (XAS) methods, which can provide crucial structural information to verify the existence of these ferromagnetic phases. The two methods, XANES (X-Ray Absorption Near

---

[1]Electromagnetic unit (emu).

2

Edge Structure) and EXAFS (Extended X-Ray Absorption Fine Structure), represent the powerful tool for the investigation of atomic and molecular structures of materials which enable direct measurements of valence state and local structure around atoms of a selected type in the sample - in our case dopants in the crystal structure of semiconducting oxides [8].

2. Experimental Setup

$BaTi_{1-x}Fe_xO_{3-x/2}$ (x = 0.02, 0.05, 0.1) ceramics were prepared using solid state reaction technique. High-purity $BaCO_3$ (99.8 %), Fe_2O_3 (99.945 %) and TiO_2 (99.9 %) powders were mixed by grinding in planetary mill at 200 rpm[2] for 1 hour. After mixing pellets were pressed by press[3] with diameter 8 mm and thickness of 3–4 mm under pressure 1 ton. Pellets were calcinated at 1000 °C for 5 hours in oxygen atmosphere. After calcination pellets were crashed and were ground once more in planetary mill at 200 rpm for 1 hour. The calcined powders were pressed into pellets under the same conditions like before calcination and were sintered at 1250 °C for 5 hours in oxygen atmosphere.

Phase identification of the sintered ceramics was performed on Panalytical x-ray diffractometer[4] with Cu Kα radiation with a step size 0.01°. The XRD patterns were recorded in the range 2θ=15–90°.

Measurements of the X-Ray absorption spectra were performed on beamline C of the laboratory Hamburger Synchrotronstrahlungslabor (HASY-LAB) at Deutsches Elektronen-Synchrotron (DESY) in Hamburg. The samples for XAS measurements were prepared in the form of homogeneous pellets with optimal absorption thickness of about 2 (absorption thickness μd=2) above the investigated Fe K-edge. The Fe-doped $BaTiO_3$ was mixed with boron nitride powder to obtain thick enough pellets. A Si(111) double-crystal monochromator was used with 0.5 eV resolution at the Fe K-edge (7112 eV). The absorption spectra were collected within [-250 eV to 788 eV] interval with respect to the Fe K-edge (Fig. 2). The three ionization chambers were filled with 1000 mbar N_2, 380 mbar Kr, and 580 mbar Kr for Fe EXAFS. Samples were placed between first and second ionization chambers.

---

[2]Rotation per minute (rpm).

[3]LP-15 Press manufactured by Lightpath Optical Ltd. at Devon, England.

[4]X'Pert Powder x-ray diffractometer manufactured by PANalytical at Almelo, Netherlands.

The exact energy calibration was established with a simultaneous absorption measurements on the Fe metal foil placed between second and third ionization chambers. The X-ray absorption spectra (EXAFS and XANES) were measured in fluorescence detection technique at room temperature.

3. Results and Discussion

3.1. X-ray diffraction

XRD was used for phase identification of the prepared samples. Fig. 1 presents XRD patterns of Fe-doped $BaTiO_3$. The standard XRD pattern of $BaTiO_3$ with hexagonal and tetragonal structures are presented at the bottom on the Fig. 1. The XRD data indicates structural differences in three samples. $BaTi_{0.98}Fe_{0.02}O_{2.99}$ has pure tetragonal perovskite structure, while $BaTi_{0.95}Fe_{0.05}O_{2.975}$ and $BaTi_{0.9}Fe_{0.1}O_{2.95}$ exhibit both tetragonal and hexagonal perovskite structures.
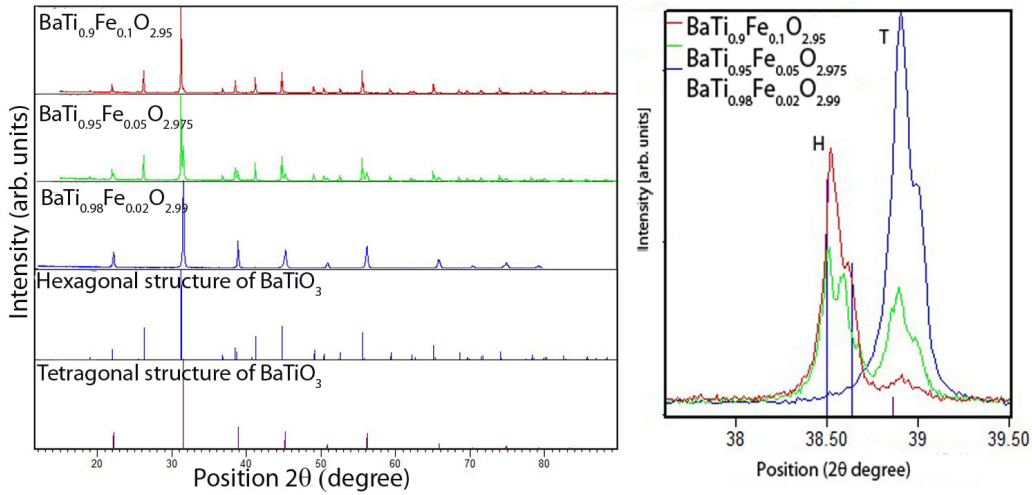
Figure 1: XRD patterns of $BaTi_{0.9}Fe_{0.1}O_{2.95}$, $BaTi_{0.95}Fe_{0.05}O_{2.975}$, $BaTi_{0.98}Fe_{0.02}O_{2.99}$, and standart pattern of $BaTiO_3$ with corresponding hexagonal and tetragonal structure (left figure). Peaks are placed in the $38.5°$ for all samples of Fe-doped $BaTiO_3$ and standard XRD patterns of pure $BaTiO_3$ are magnified in the right figure. On the right figure is presented increasing of the hexagonal peaks (H peaks) and in the same time decreasing of the tetragonal peaks (T peaks) with exceeding amount of iron dopant.

Comparison of $BaTi_{0.95}Fe_{0.05}O_{2.975}$ and $BaTi_{0.9}Fe_{0.1}O_{2.95}$ XRD patterns shows exceeding amount of Fe dopant reduces peaks of tetragonal structure and in the same time increase peaks of hexagonal structure (Fig. 1). XRD does not indicate other additional peaks, but XRD is not very sensitive method to indicate the existence of clusters or secondary phases.

3.2. X-ray absorption spectroscopy

X-ray spectroscopy method was used to investigate the Fe valence state and local environments. Fe K-edge of $BaTi_{0.98}Fe_{0.02}O_{2.99}$ X-ray absorption spectra was measured (Fig. 2). The shape of the edge and the pre-edge region are characteristic for the local symmetry of the investigated atom sites. There is a weak resonance in the pre-edge region in the XANES spectra of the iron (Fig. 2). Thus, iron atoms are octahedraly coordinated by six oxygen atoms.
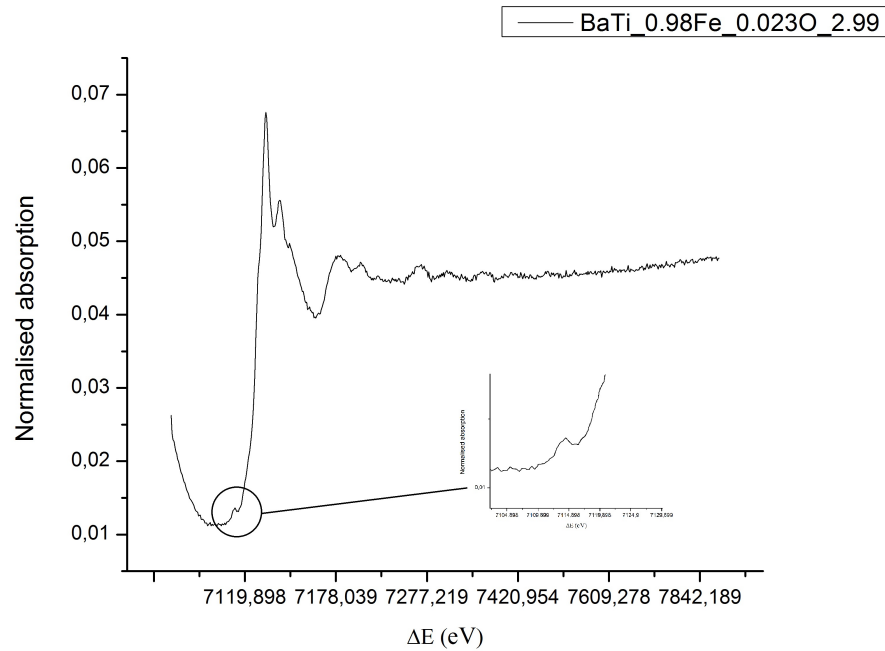
Figure 2: The Fe K-edge spectra of the model $BaTi_{0.98}Fe_{0.02}O_{2.99}$. Weak resonance in the pre-edge region, magnified in the inset, is feature in identification of the octahedral symmetry of the iron atom.

5

The energy position of the Fe K-edge are correlated with valence state of the iron atom in the $BaTi_{0.98}Fe_{0.02}O_{2.99}$. Fig. 3 presents XANES spectra of $BaTi_{0.98}Fe_{0.02}O_{2.99}$ and XANES spectra of different compounds with well established Fe^{2+} and Fe^{3+} valence states. There are Fe_2O_3, FeOOH as references for Fe^{3+} and $FeSO_4$, $LiFePO_4$ as references for Fe^{2+}. Comparison of positions of the Fe K-edge shows that $BaTi_{0.98}Fe_{0.02}O_{2.99}$ K-edge belong to set of compounds with valence state Fe^{3+}. Thus, the Fe valence in the synthesized sample is 3+.
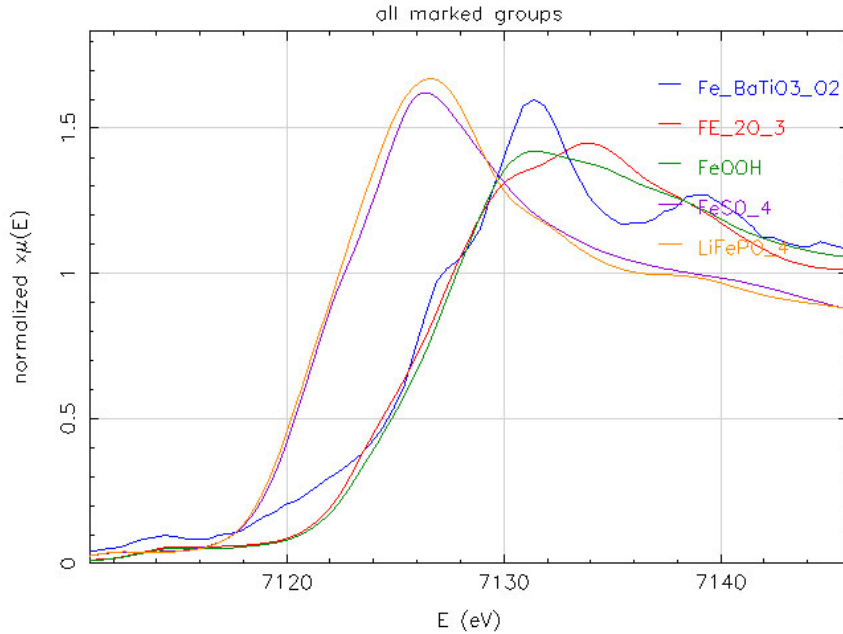
Figure 3: Comparison of the Fe K-edge XANES spectra of $BaTi_{0.98}Fe_{0.02}O_{2.99}$ and reference samples with well established Fe^{2+} (Fe_2O_3, FeOOH) and Fe^{3+} ($FeSO_4$, $LiFePO_4$) valence states.

Fourier transformation EXAFS spectra can be used for determination of radial distribution of the neighbors. Fig. 4 presents Fourier transformation of Fe K-edge and Ba L_3-edge EXAFS spectra of $BaTi_{0.98}Fe_{0.02}O_{2.99}$. From qualitative analysis is evident that Fourier transformations are different, and we assume that Fe^{3+} ions substituted Ti^{4+} sites (Fig. 4).

To verify our assumptions we used quantitative EXAFS analysis. From quantitative EXAFS analysis can be obtained structural information of the
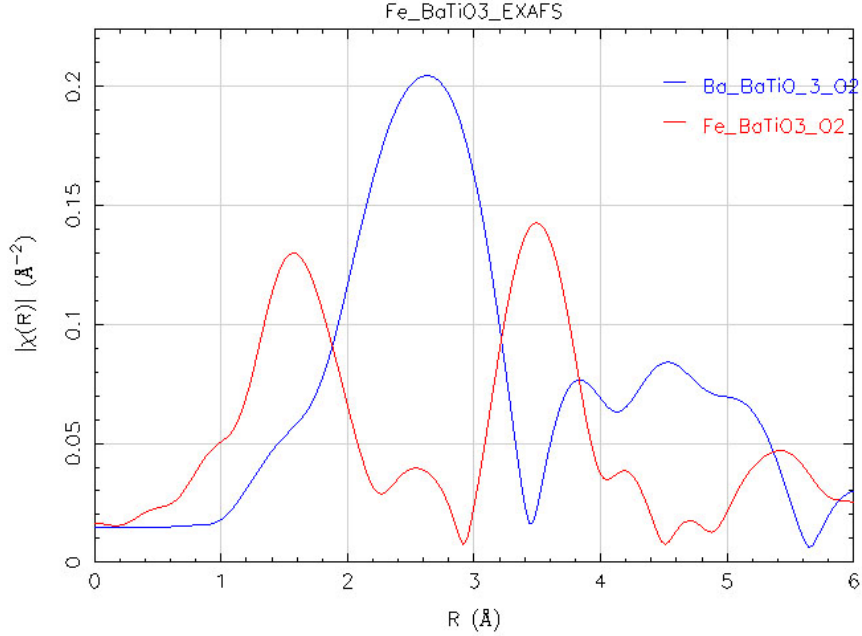
Figure 4: Comparison of the Fe K-edge and Ba L_3-edge Fourier transform magnitudes measured for $BaTi_{0.9}Fe_{0.1}O_{2.95}$. Fe^{3+} ions substituted Ti^{4+} sites.

local environment (number and species of neighboring atoms). In the simultaneous fit of EXAFS signal of $BaTi_{0.98}Fe_{0.02}O_{2.99}$, a nearly perfect fit was obtained, using the k-interval of $[4$–11 Å$^{-1}]$ (Fig. 5). Debye-Waller (the mean square variation in bond length) remain within reasonable limits $0.007(3)$ Å^2 for the first shell. The fitting parameters are summarized in the Table 1. Quantitative EXAFS analysis showed that Fe atoms substituted Ti^{4+} site and dissolved in the $BaTiO_3$ host matrix. No impurities or secondary phases were observed.

Table 1: Fitting parameters. First and second columns present species and number of Fe neighbors, third column presents their distance from absorbing atom and the fourth column presents Debye-Waller factor. In brackets specified relative error.

Type	Number	Distance, Å	Debye-Waller factor
O	4	2.05(1±0.029)	0.007(1±0.429)
O	2	2.00(1∓0.005)	0.007(1±0.429)
Ba	8	3.45(1∓0.006)	0.008(1±0.125)
Ti	4	3.97(1∓0.005)	0.008(1±0.375)
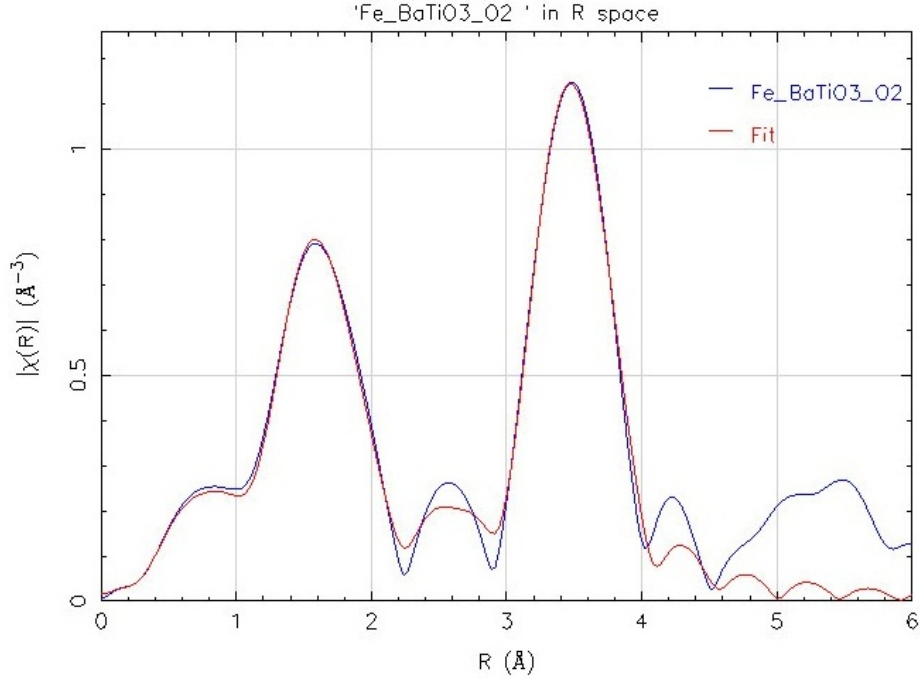
Figure 5: Best fit of Fe K-edge EXAFS using k-interval of [4–11 Å^{-1}] and k^2 weight at room temperature. Blue line denote the experiment and red line the EXAFS model prediction.

4. Conclusion

Within this work Fe doped $BaTiO_3$ was synthesized by solid state reaction. From XRD analysis we have found that samples have different crystal structures: $BaTi_{0.98}Fe_{0.02}O_{2.99}$ has tetragonal perovskite structure, $BaTi_{0.95}Fe_{0.05}O_{2.975}$ and $BaTi_{0.9}Fe_{0.1}O_{2.95}$ exhibit both tetragonal and hexagonal perovskite structures. We observed reduction of amplitude of tetragonal peaks with increasing amount of Fe^{3+} ions. However, we can not determine the place of Fe dopant in host matrix of $BaTiO_3$ by XRD. For solving this problem X-ray absorption method was used. From quantitative EXAFS analysis we can say that no impurities, such as clusters or ferromagnetic phases, were observed. Thus Fe dopant completely dissolved in $BaTiO_3$ host matrix and substituted Ti^{4+} sites.

References

[1] V.A. Ivanov, T.G. Aminov, V.M. Novotortsev, V.T. Kalinnikov. *Spintronics and spintronics materials*, Russion Chemical Bulletin, International Edition, 53 pp. 2357-2405, 2004.

[2] QIU Shen-yu, LI Wang, LIU Yu, LIU Gui-hua, WU Yi-qianz, CHEN Nan. *Phase evolution and room temperature ferroelectric and magnetic properties of Fe-doped BaTiO₃ ceramics*, Trans. Nonferrous Met. Soc. China, 20 pp. 1911-1915, 2010.

[3] F. Lin, D. Jiang, X. Ma, W. Shi. *Influence of doping concentration on room-temperature ferromagnetism for Fe-doped BaTiO₃ ceramics*, Journal of Magnetism and Magnetic Materials, 320 pp. 691-694, 2007.

[4] E. Mashkina, C. McCammon, F. Seifert. *A Mo̎ssbauer study of oxygen vacansy and cation distribution in 6H-BaTi₁₋ₓFeₓO₃₋ₓ/₂*, Journal of Solid State Chemistry, 177 pp. 262-267, 2003.

[5] S. Ray, P. Mahadevan, S. Mandal, S.R. Krishnakumar, C.S. Kuroda, T. Sasaki, T. Taniyama, M. Itoh. *High temperature ferromagnetism in single crystalline dilute Fe-doped BaTiO₃*, Physical review, B 77 p. 104416, 2008.

[6] N. Zhang, J.F. Fan, X.F. Rong, H.X. Cao, J. Wei. *Magnetoelectric effect in laminate composites of Tb₁₋ₓDyₓFe₂₋ᵧ and Fe-doped BaTiO₃*, Journal of Applied Physics, 101 (6) p. 06397, 2007.

[7] K. Yates. *Dilute magnetic oxides*, The Blacket Laboratory, Physics Department, Imperial College London.

[8] I. Arčon. *Introduction to XANES and EXAFS analysis*, University of Nova Gorica, 2008.

Study of ionospheric scintillations in the African region using satellite signals

Andreja Sušnik

University of Nova Gorica, Vipavska 13, SI-5000 Nova Gorica

Abstract

A sample of ionospheric scintillation activity measured in the African region (Douala, Cameroon, magnetic latitude 5.36°N) by means of Global Navigation Satellite System (GNSS) signals is analyzed.

The measurements consist of classical ionospheric scintillation indices evaluated at the L_1(1575.42 MHz) and L_2 (1227.60 MHz) band by means of a dedicated dual frequency GPS receiver (GSV4004) capable of estimating the temporal fluctuations superimposed on the radio signals by drifting plasma density inhomogeneities. The experimental campaign refers to the period from March 2004 to February 2005. The analysis confirmed the well know seasonal and diurnal variation of scintillation activity in the African region.

Keywords: ionosphere, equatorial scintillation, Global Navigation Satellite System

1. Introduction

The ionosphere represents the ionized portion of the upper atmosphere. It extends from about 60 km to beyond 1000 km in height and completely encircles the Earth. The main source of ions and electrons in the ionosphere is photoionization of neutral molecules by the solar EUV (Extreme Ultraviolet) and soft X-ray radiation, although other production processes may dominate in certain region [1, 2]. Due to the variation of the electron density with altitude, the ionosphere is vertically "organized" (Fig. 1) in layers D, E and F [1, 3], where the D layer extends from $\approx$ 60 km to 90 km altitude, the E layer extends from 90 km to 140 km altitude and the F layer from 140 km to

1000 km altitude. At the uppermost altitudes the ionosphere merges with the magnetosphere of the Earth.

The electron density in all regions varies with the time of day, season, solar cycle and level of magnetosphere or solar wind disturbance. The variation of electron density with the time of day is shown on Fig. 1 a), where the peak plasma density occurs in F–layer near noon local time.

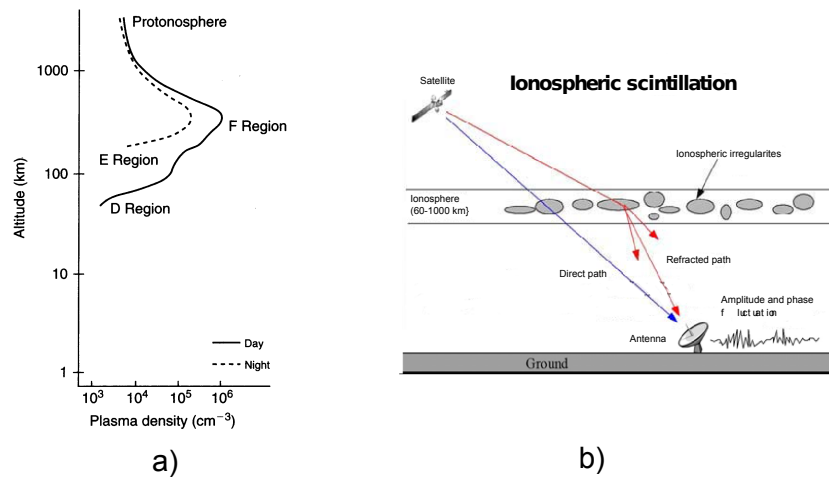Figure 1: a) Ion density profile for the nighttime and daytime ionosphere[1] and b) schematic diagram of ionospheric scintillation and its effects on satellite signals (reproduced version of figure in [4] without tropospheric effects).

It is well known that trans-ionospheric radio signals, such as satellite signals, may experience fluctuations in their amplitude and phase due to irregularities in the spatial electron density distribution, referred to as scintillation [5]. Ionospheric scintillation can cause signal power fading, phase cycle slips, loss of receiver lock etc., and can degrade the quality of satellite navigation systems. The schematic diagram of scintillations is shown in Fig. 1 b). Global morphology of scintillation activity shows us that scintillation activity is intense in the equatorial regions and strong in the high latitudes while in the middle latitudes it appears to be weak [6]. From Fig. 2 it can be also seen that intensity of scintillation has a temporal dependence [3], according to the solar cycle, local season and time of day. Scintillation occurring in the equatorial region is also known as equatorial scintillation and usually takes place after the sunset [3]. This post-sunset occurrence of scintillation activity is due to the so-called Equatorial Anomaly which is present in regions where the electron density is enhanced. It is indicated with $\mathbf{E} \times \mathbf{B}$ drift, which drives the electron plasma upward. This plasma

is then diffused along the **B** field under the influence of gravity and the pressure gradient. This process happens in the daylight hemisphere, but at dusk the electric field **E** increases when the neutral winds increase. The consequence of this process is that the $\mathbf{E} \times \mathbf{B}$ drift raises the F-layer. This process is known as Pre-Reversal Enhancement which leads to the scintillation occurring in the night–time [3].
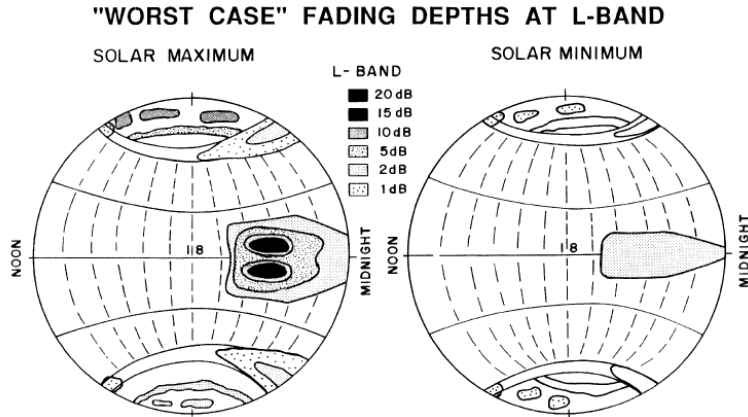

Figure 2: Schematic of the global morphology of scintillations at L-band frequencies during the solar maximum (left panel) and solar minimum (right panel) conditions [6].

The aim of this paper is to show how scintillation activity varies with season, time of day and satellite path in the sky in the African region.

2. Experimental setup

The data used in this analysis were collected with the GPS Ionospheric Scintillation and TEC Monitor (GISTM) stationed in a near-equatorial location in Africa (Douala, Cameroon – 4° 00' 49.5756" East Latitude, 9° 42' 55.4544" North Longitude, and 48.3 m altitude), see Fig. 3. The receiver (GSV4004) measures phase, amplitude (at 50 Hz rate) and code/carrier divergence (at 1 Hz rate) on 12 channels for each satellite being tracked on the L_1 band (1575.42 MHz) and the L_2 band (1227.60 MHz). The Total Electron Content (TEC) is then computed from combined L_1 and L_2 pseudo-range and carrier phase measurements. While 11 channels are used for tracking and measuring data from GNSS satellites, the 12th channel is configured for tracking Satellite-based Augmentation System Satellites (SBAS) and is also being used for measuring noise level for S/N_0 and S_4 correction computations [7, 8].
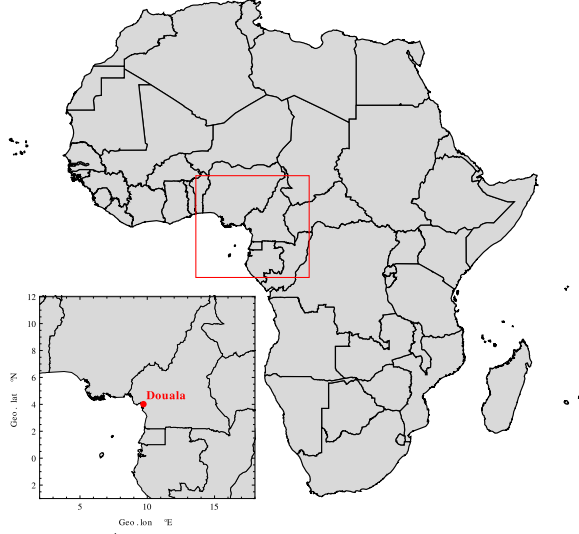
Figure 3: Geographical location of Douala.

To measure scintillation activity one can use various different parameters. One of these parameters, used for measuring ionospheric amplitude scintillation, is S_4 index. S_4 index is derived from the signal intensity of signals received from satellites and is defined [8, 9, 10] as the normalized standard deviation of the received signal power intensity expressed as

$$S_4 = \sqrt{\frac{\langle I^2 \rangle - \langle I \rangle^2}{\langle I \rangle^2}}. \tag{1}$$

S_4, defined in Eq. (1), measured at the L band needs to have the effects due to ambient noise removed, since the ambient noise at the L_1 frequency can translate to relatively high S_4 values at lower VHF and UHF frequencies [8, 9, 10]. This can be carried out by estimating the average signal–to–noise density over the entire evaluation interval (60 s), and using this estimate to determine the expected S_4 due to ambient noise. If the signal–to–noise density (S/N_0) is known, the predicted S_4 due to the ambient noise can be expressed as

$$S_{4N_0} = \sqrt{\frac{100}{S/N_0} \left[1 + \frac{500}{19 \, S/N_0} \right]}. \tag{2}$$

By replacing S/N_0 with the 60 s estimated signal-to-noise density $\hat{S}/\hat{N}_0$ in

4

69   Eq. (2), we obtain an estimate of the S_4 due to noise S_{4N_0} [9]

$$S_{4\hat{N}} = \sqrt{\frac{100}{\hat{S}/\hat{N}_0}\left[1 + \frac{500}{19\,\hat{S}/\hat{N}_0}\right]}. \tag{3}$$

70   Subtracting the Eq. (3) from Eq. (1) yields the corrected value of S_4 as fol-
71   lows [9]

$$S_4 = \sqrt{\frac{\langle I^2\rangle - \langle I\rangle^2}{\langle I\rangle^2} - \frac{100}{\hat{S}/\hat{N}_0}\left[1 + \frac{500}{19\,\hat{S}/\hat{N}_0}\right]}. \tag{4}$$

72

73   The second most frequently used parameter is the so-called phase scintil-
74   lation index σ_ϕ. Phase scintillation is obtained by monitoring the standard
75   deviation, σ_ϕ, of the detrended carrier phase from signals received from
76   satellites [11]. The receiver calculates the standard deviation in real-time
77   over 1, 3, 10, 30 and 60 second intervals every 60 seconds, using the 50 Hz
78   detrended phase measurements. The σ_ϕ for 1, 3, 10 and 30 second interval
79   are then averaged over the 60 second interval, which gives the scintillation
80   activity for each satellite begin tracked during that minute [11]. To elim-
81   inate σ_ϕ collected before the phase detrending filter has converged, one
82   must discard all σ_ϕ with lock time less than 240 seconds and with very
83   large values. This will prevent any confusion between "false" and legiti-
84   mate scintillation events obtained with σ_ϕ.

85

86   The correct value of the S_4 index (S_4 without ambient noise) used in this
87   analysis was calculated using the equations described above. For eliminat-
88   ing all the σ_ϕ collected before the phase detrending filter has converged,
89   the data with lock time less than 240 seconds and value of σ_ϕ greater than 1
90   were discarded. Furthermore, to discard all the effects that the troposphere
91   might have on the signal, a satellite elevation cut-off of 20° was used.

92   **3. Discussion and conclusions**

93   The overall picture of scintillation activity in the African region is shown
94   in Fig. 4 and Fig. 5. Figure 4 presents the percentages of $S_4 > 0.2$, while
95   Fig. 5 presents the percentages of $\sigma_\phi > 0.2$ for the entire measurement cam-
96   paign.
97   From Fig. 4 it can be seen that there is a pronounced scintillation activ-
98   ity, measured with the S_4 index, between March and May (near equinoxes),
99   especially between 28th March and 3th April, while there are very low val-
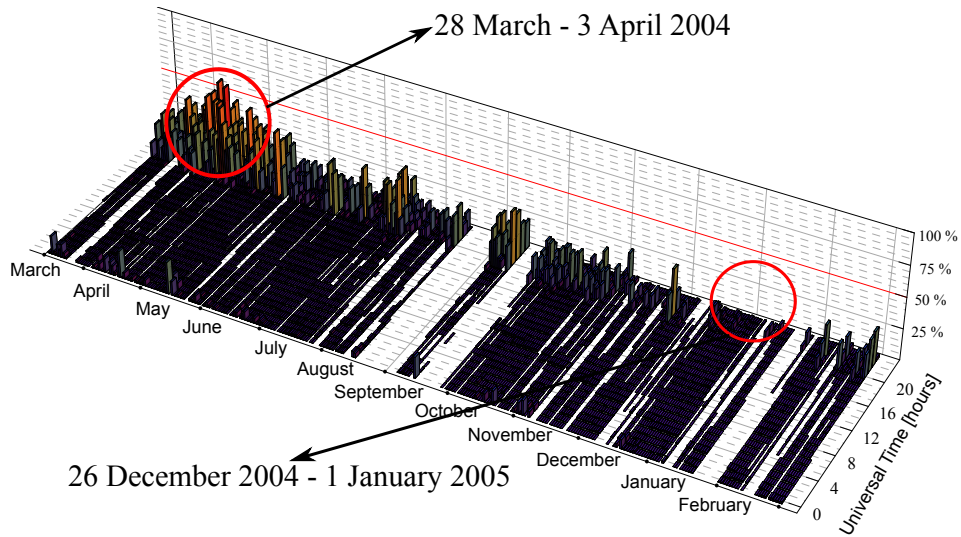100   ues between December and February, especially between 26th December

Figure 4: Percentages of $S_4 > 0.2$ between March 2004 and February 2005.
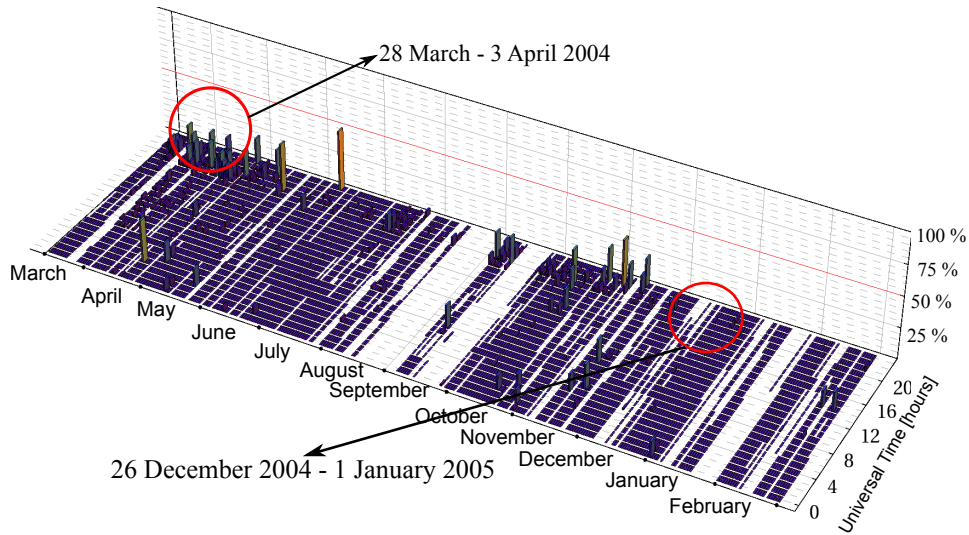

Figure 5: Percentages of $\sigma_\phi > 0.2$ between March 2004 and February 2005.

and 1th January. The same maximum and minimum periods of scintillation activity can be seen in Fig. 5 for σ_ϕ index. This two peaks (maximum and minimum) in Fig. 4 and Fig. 5 correspond well with the known seasonal variations in scintillation activity. Almost 50% of all events had $S_4 >$

6

105 0.2. On the other hand there are very low values between December and
106 February, especially between the 26$^{\text{th}}$ of December and the 1$^{\text{th}}$ of January
107 were there are almost no events with $S_4 > 0.2$. σ_ϕ follows well the S_4 index
108 but the values expressed in % are much lower than for S_4. This shows that
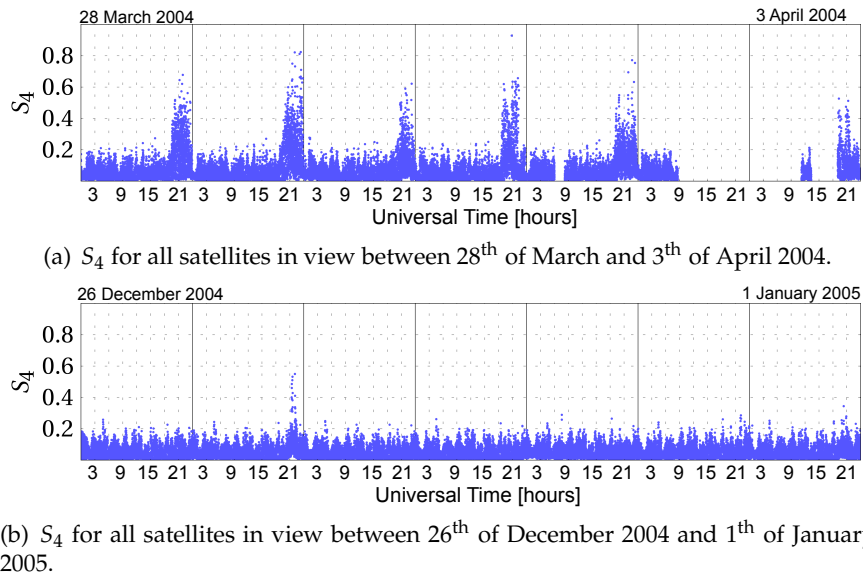109 the scintillation had rather more effect on the amplitude of the signal than
110 on the phase.

(a) S_4 for all satellites in view between 28$^{\text{th}}$ of March and 3$^{\text{th}}$ of April 2004.

(b) S_4 for all satellites in view between 26$^{\text{th}}$ of December 2004 and 1$^{\text{th}}$ of January 2005.
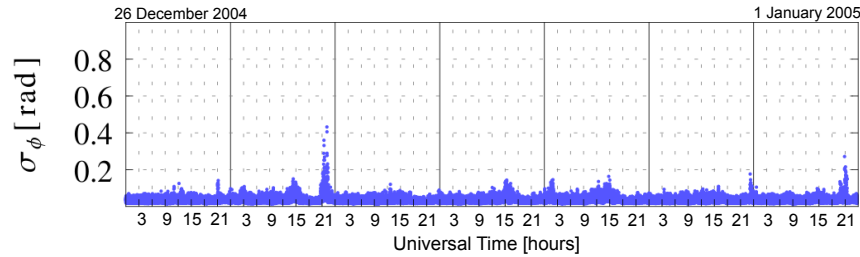
Figure 6: S_4 for both periods under consideration.

111   In addition to the clear seasonal variation of scintillation activity, there
112 is also pronounced activity in the night-time, especially during the equinoxes
113 between 18 UT (Universal Time) and 24 UT (Fig. 6, 7). This night-time ac-
114 tivity is due to the pre-reversal enhancement. Figure 6 presents the S_4 for
115 all satellites in view during both periods, while Fig. 7 presents the value of
116 σ_ϕ for all satellites that were in view during both periods. In both figures
117 the upper panel (Fig. 6(a) and Fig. 7(a)) presents the period of the maxi-
118 mum of the scintillation activity and the lower panel (Fig. 6(b) and Fig. 7(b))
119 presents the period with minimum of scintillation activity. As can be no-
120 ticed from Figs. 6 and 7 the pronounced scintillation activity was much
121 higher during the maximum peak of activity. The majority of scintillation
122 started at $\approx$ 18 UT and lasted to $\approx$ 24 UT. Although σ_ϕ is following the S_4,
123 there is additional phase scintillation observed ($\approx$ 15 UT). This additional
124 peak phase scintillation activity is probably due to the geometry of the sig-
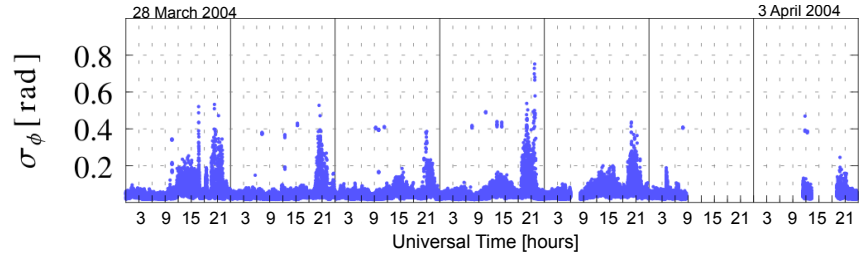
7

(a) σ_ϕ for all satellites in view between 28$^{\text{th}}$ of March and 3$^{\text{th}}$ of April 2004.

(b) σ_ϕ for all satellites in view between 26$^{\text{th}}$ of December 2004 and 1$^{\text{th}}$ of January 2005.

Figure 7: σ_ϕ for both periods under consideration.

nal of the satellite on the sky, but additional analysis of this phenomena is being carried out. On the other hand, there was almost no nighttime maximum observed in the December period except on the 27$^{\text{th}}$ of December (Fig. 6(b) and Fig. 7(b)).

Figure 8 denotes the value of S_4 and σ_ϕ for satellite with PRN number 4 on 29$^{\text{th}}$ March. PRN stands for pseudo-range code and presents the "name" of the satellite. In Fig. 8(a) the values of S_4 and σ_ϕ are plotted together with the elevation of the satellite, while in Fig. 8(b) their trajectory path over Douala – so called sky-plot – is shown. The color here follows the value of each index, i.e blue is 0 and red the highest value (for S_4 this value is 0.8 and for σ_ϕ 0.4). As can be noticed from Fig. 8(a) the scintillation started to occur when the satellite was at the 90° of elevation ($\approx$ 20 UT). This corresponds well with the Fig. 8(b) and with enhanced night-time scintillation activity.
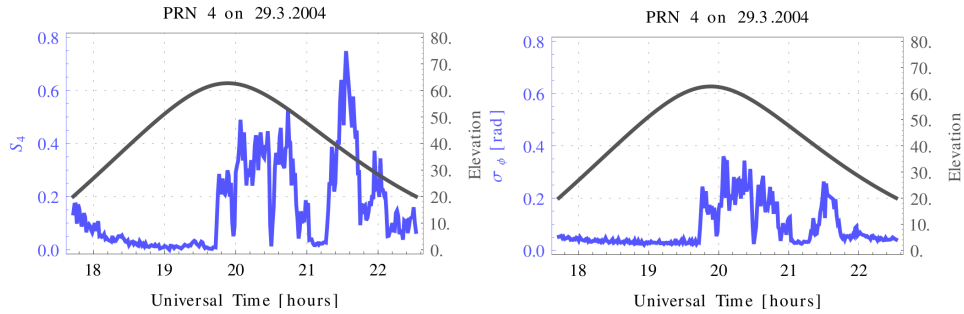
(a) S_4 (left) and σ_ϕ (right) for PRN 4 plotted with elevation of the satellite.
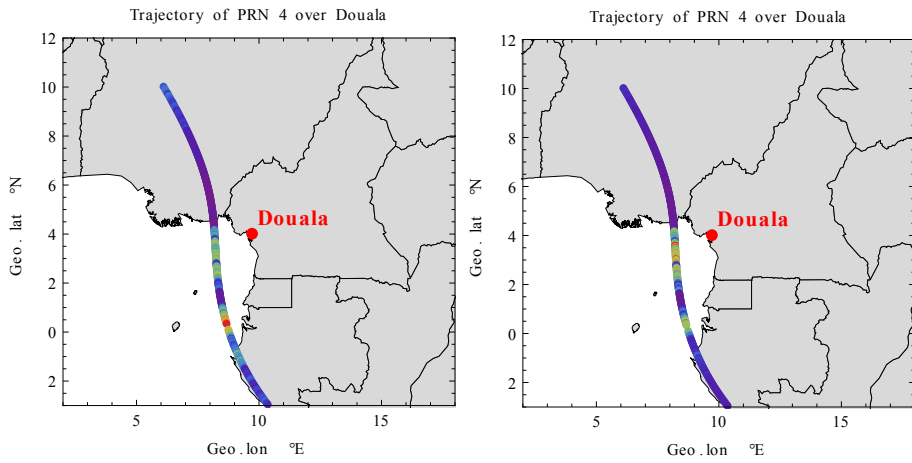
(b) Satellite path over Douala where value of the color present the value of S_4 (left) and σ_ϕ (right).

The data used in this analysis confirmed the well know seasonal and diurnal variation of scintillation activity in the African region. It has been shown that scintillation is essentially a night-time phenomenon with enhancements during the equinoctial months.

Acknowledgments

References

[1] M.C. Kelley. *The Earth's Ionosphere: plasma physics and electrodynamics*, Second Edition, 2009.

[2] R.W. Schunk, A.F. Nagy. *Ionosphere: physics, plasma physics and chemistry*, 2000.

[3] A. de Oliveira Moraes, W.J. Perrella. *Performance evaluation of GPS receiver under equatorial scintillation*, Journal of Aerospace Technology and Management, V. 1, n. 2, pp. 193–199, 2009.

[4] P. Theerapatpaiboon, S. Sukkaewthanom, N. Leelaruji and N. Hemmakorn. *The study of scintillation on C-band low elevation angle at Sri-Racha satellite Earth station*, Proceedings of ICCAS2004.

[5] A. Sušnik, B. Forte, V. Romano. *Effects of magnetic storms on GPS signals at high latitudes in the European sector*, EGU2011.

[6] S. Basu, K.M. Groves, Su. Basu, P.J. Sultan. *Specification and forecasting of scintillations in communication/navigation links: current status and future plans*, Journal of Atmospheric and Solar-Terrestial Physics 64, pp. 1745–1754, 2002.

[7] GSV4004B. *GPS Ionospheric Scintillation & TEC Monitor, (GISTM)*, User's manual, August 2007.

[8] M.T.A.H. Muella, E.R. de Paula, I.J. Kantor, I.S. Batista, J.H.A. Sobral, M.A. Abdu, P.M. Kintner, K.M. Groves and P.F. Smorigo. *GPS L–band scintillations and ionospheric irregularity zonal drifts inferred at equatorial and low–latitude regions*, Journal of Atmospheric and Solar–Terrestrial Physics, 70 pp. 1261–1272, 2008.

[9] A. J. Van Dierendock, J. Klobuchar and Q. Hua. *Ionospheric Scintillation Monitoring Using Commercial Single Frequency C/A Code Receivers*, ION GPS-93 proceedings: 6 international technical meeting of the satellite division of the Institute of Navigation, Institute of Navigation, Salt Lake City, Utah, pp. 13331342, 1993.

[10] M. Abdullah, A. F. M. Zain, Y. H. Ho and S. Abdullah. *TEC and Scintillation Study of Equatorial Ionosphere: A Month Campaign over Sipitang and Parit Stations, Malaysia*, American Journal of Engineering and Applied Sciences 2 (1): pp. 44-49, ISSN 1941–7020, 2009.

[11] A. J. Van Dierendonck, B. Arbesser-Rastburg. *Measuring Ionospheric scintillation in the equatorial region over Africa, including measurements from SBAS geostationary satellite signals*, Proceeding of ION GNSS 17th technical meeting of the satellite division, Long Beach, CA, 316, 2004.